Diverse Cell Stimulation Kinetics Identify Predictive Signal Transduction Models

Hossein Jashnsaz, Zachary Fox, Jason Hughes, Guoliang Li, Brian Munsky, Gregor Neuert

iScience

CellPress
OPEN ACCESS

Article

Diverse Cell Stimulation Kinetics Identify Predictive Signal Transduction Models

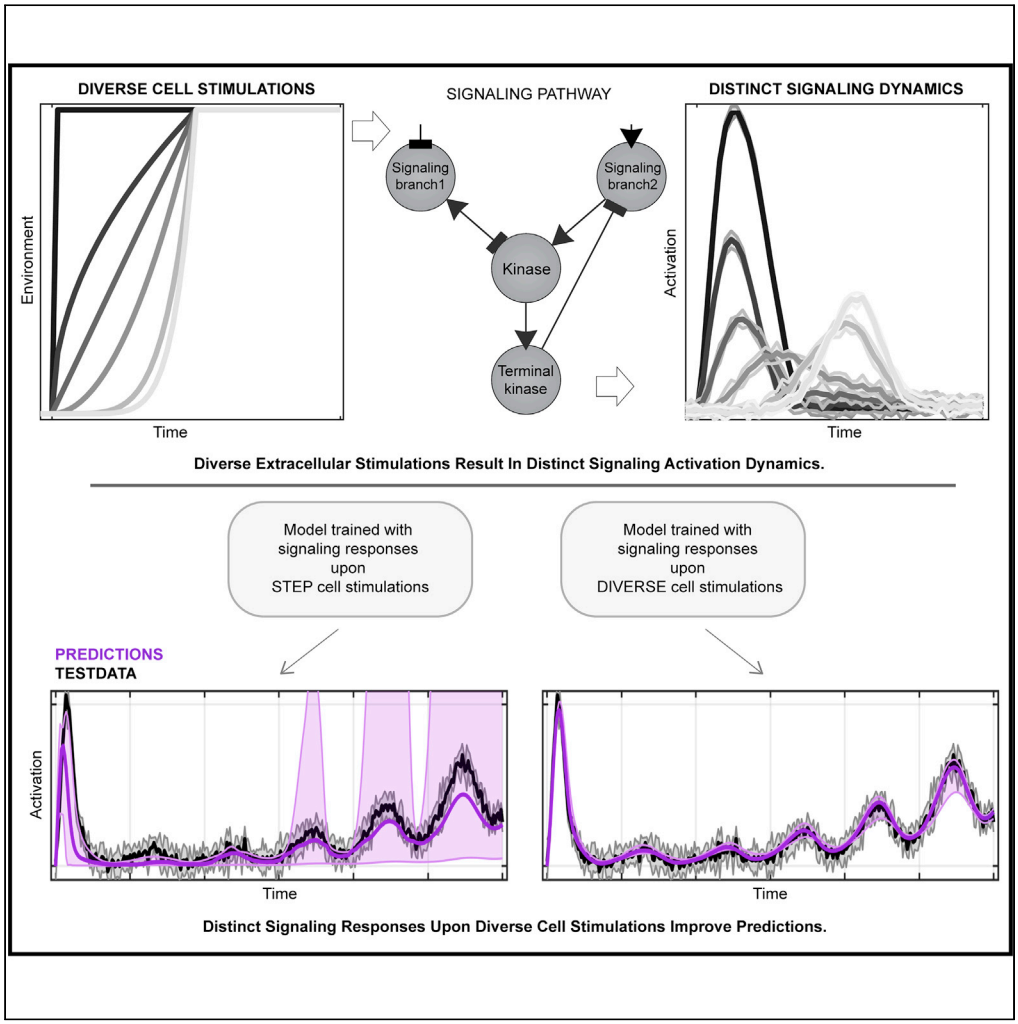

Hossein Jashnsaz, Zachary R. Fox, Jason J. Hughes, Guoliang Li, Brian Munsky, Gregor Neuert

brian.munsky@colostate.edu (B.M.)
gregor.neuert@vanderbilt.edu (G.N.)

HIGHLIGHTS

Diverse kinetic cell stimulations result in distinct signaling response dynamics

Diverse kinetics compared with step stimulations better constrain model parameters

Diverse kinetic stimulations improve predictions of WT and mutant pathway responses

Diverse kinetic stimulations compared with steps discriminate competing signaling models

Jashnsaz et al., iScience *23*, 101565
October 23, 2020
https://doi.org/10.1016/j.isci.2020.101565

iScience

CellPress
OPEN ACCESS

Article

Diverse Cell Stimulation Kinetics Identify Predictive Signal Transduction Models

Hossein Jashnsaz,[1] Zachary R. Fox,[2,3,4] Jason J. Hughes,[1] Guoliang Li,[1] Brian Munsky,[4,5,*] and Gregor Neuert[1,6,7,8,*]

SUMMARY

Computationally understanding the molecular mechanisms that give rise to cell signaling responses upon different environmental, chemical, and genetic perturbations is a long-standing challenge that requires models that fit and predict quantitative responses for new biological conditions. Overcoming this challenge depends not only on good models and detailed experimental data but also on the rigorous integration of both. We propose a quantitative framework to perturb and model generic signaling networks using multiple and diverse changing environments (hereafter "kinetic stimulations") resulting in distinct pathway activation dynamics. We demonstrate that utilizing multiple diverse kinetic stimulations better constrains model parameters and enables predictions of signaling dynamics that would be impossible using traditional dose-response or individual kinetic stimulations. To demonstrate our approach, we use experimentally identified models to predict signaling dynamics in normal, mutated, and drug-treated conditions upon multitudes of kinetic stimulations and quantify which proteins and reaction rates are most sensitive to which extracellular stimulations.

INTRODUCTION

One of the longest standing challenges of modeling in systems biology has been to make accurate quantitative predictions for cell signaling responses over time, upon genetic mutations, when subjected to variable drug concentrations, and under time-varying changes of environment (Fujita et al., 2010; Handly et al., 2016; Rowland et al., 2011; Sorre et al., 2014; Lim and Bruce Mayer, 2017). Examples of environmental perturbations that change over time that cells experience (defined as "kinetic stimulations") include changes in levels of hormones (Kubota et al., 2012; Steiner et al., 1982), growth factors (Fujita et al., 2010; Sorre et al., 2014), morphogens (Briscoe and Small, 2015; Huang et al., 2017), cytokines (Oyler-Yaniv et al., 2017), or extracellular stressors such as oxidative stress (Goulev et al., 2017) or osmolarity (Granados et al., 2017; Mitchell et al., 2015; Young et al., 2013). These environmental changes can modulate signaling dynamics in pathways in both healthy and disease tissue (Akhurst and Hata, 2012; Cildir et al., 2016; Hanahan and Weinberg, 2000; Hata and Chen, 2016; Hotamisligil and Davis, 2016). Therefore, understanding and predicting signal transduction network behavior will be a critical step to identify unknown regulatory mechanisms, to distinguish between proteins and reaction rates that are sensitive to kinetic stimulations, and to detect and treat abnormal regulation that occurs in a large number of human diseases.

A key obstacle that prevents predictive modeling of cell signaling is the gross mismatch between the preponderance of biological complexity and the sparsity of quantitative experimental data (Handly et al., 2016; Janes and Lauffenburger, 2013; Vanhaelen et al., 2017). As a consequence, most current models of signal transduction pathways suffer from lack of dynamic richness in the data resulting in either too simple (Adler and Alon, 2018; Csete and Doyle, 2002; Muzzey et al., 2009) or too complex (Groβ et al., 2019; Klipp et al., 2005; Romers et al., 2020) models with limited predictive power (Handly et al., 2016; Janes and Lauffenburger, 2013). To address the disparity between biological complexity and lack of richness in experimental data, one paradigm has been to devise experiments with higher content (e.g., sequencing or multiplexed single-cell imaging) or higher throughput (e.g., flow cytometry or parallelized microfluidics) in hope that large amounts of data will eventually fill the gap between mechanistic and predictive understanding (Efremova et al., 2020; Labib and Kelley, 2020). These approaches have been helpful to quantify RNA or protein abundances or phosphorylation states of many proteins using the minimal number of time points to better

[1]Department of Molecular Physiology and Biophysics, School of Medicine, Vanderbilt University, Nashville, TN 37232, USA

[2]Inria Saclay Ile-de-France, Palaiseau 91120, France

[3]Institut Pasteur, USR 3756 IP CNRS, Paris 75015, France

[4]Keck Scholars, School of Biomedical Engineering, Colorado State University, Fort Collins, CO 80523, USA

[5]Department of Chemical and Biological Engineering, Colorado State University, Fort Collins, CO 80523, USA

[6]Department of Biomedical Engineering, School of Engineering, Vanderbilt University, Nashville, TN 37232, USA

[7]Department of Pharmacology, School of Medicine, Vanderbilt University, Nashville, TN 37232, USA

[8]Lead Contact

*Correspondence: brian.munsky@colostate.edu (B.M.), gregor.neuert@vanderbilt.edu (G.N.)

https://doi.org/10.1016/j.isci.2020.101565

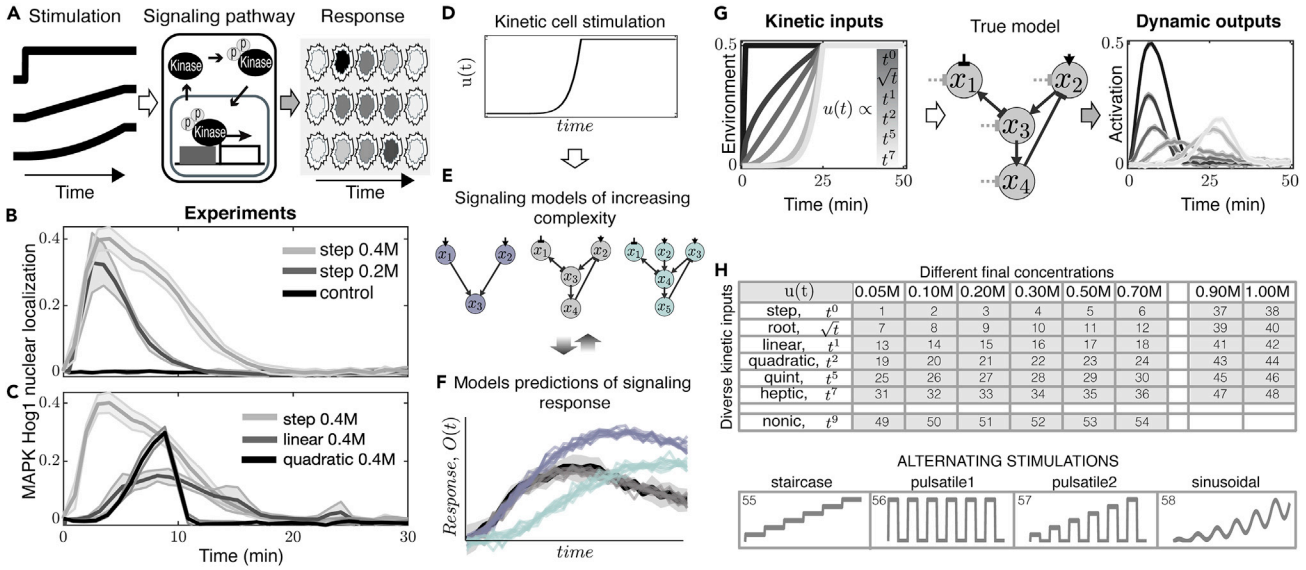

u(t)	0.05M	0.10M	0.20M	0.30M	0.50M	0.70M	0.90M	1.00M
step, t^0	1	2	3	4	5	6	37	38
root, $\sqrt{t}$	7	8	9	10	11	12	39	40
linear, t^1	13	14	15	16	17	18	41	42
quadratic, t^2	19	20	21	22	23	24	43	44
quint, t^5	25	26	27	28	29	30	45	46
heptic, t^7	31	32	33	34	35	36	47	48
nonic, t^9	49	50	51	52	53	54		

Figure 1. Kinetic Stimulation of Signaling Pathways Is Required to Identify Predictive Models and Phenotypes

(A) Different extracellular kinetic stimulations (left) activate a signaling pathway (middle) and result in distinct dynamic kinase signaling and nuclear localization (right).

(B) MAPK Hog1 nuclear localization dynamics upon step increases in NaCl to different final concentrations.

(C) Hog1 dynamics upon step, linear, or quadratic increases from 0 to 0.4 M NaCl. Lines are means, and shaded areas are the standard deviation of multiple biological replicates (Transparent Methods).

(D–F) (D) Schematic overview of model identification based on models' predictions utilizing kinetic cell stimulations. (E) Schematic overview of signaling models of different complexity where pathways are modeled with ordinary differential equations (ODE) (Figure S1; Transparent Methods). The middle model is defined as the "true model" to simulate synthetic data for pathway response (defined as the activation of node x_4). Different models were fitted to the same data to identify parameters. (F) These models were then used to make predictions for pathway activation, depicted as black solid line, upon a different kinetic input, which resulted in different responses for different models (colored lines).

(G) Diverse kinetic perturbations corresponding to step (t^0), root ($\sqrt{t}$), linear (t^1), quadratic (t^2), quint (t^5), and heptic (t^7) changes over time (left) are applied to the true model (middle) resulting in synthetic signaling activation dynamics (right). In synthetic signaling data, lines are means and shaded areas are the standard deviation of simulated replicates (Transparent Methods).

(H) Diverse kinetic inputs reaching different final concentrations plus four alternating stimulations result in 58 distinct simulated datasets for each model. These datasets are used to train models and test their predictions. The alternating stimulations include a staircase input, two pulsatile inputs, and a sinusoidal oscillatory input (Figures S3E–S3H).

See also Figures S1–S3 and Table S1.

constrain complex models (Kinney et al., 2019). Another approach has been to fit computational models to experiments at steady state in different environments (Hao and O'Shea, 2012), to dose-response curves measured with sudden step-like perturbations (Shaw et al., 2019), to repetitive pulsatile perturbations of different frequencies (Albeck et al., 2013; Ashall et al., 2009; Hersen et al., 2008; Mettetal et al., 2008; Mitchell et al., 2015; Rahi et al., 2017; Wang et al., 2012; Zhang et al., 2019), or to individual spatial gradients (Huang et al., 2017) or design optimal experiments that constrain parameters for a specific perturbation profile (Apgar et al., 2008; Bandara et al., 2009; Casey et al., 2006; Faller et al., 2003; Hagen et al., 2013). In addition, pioneering studies have further demonstrated that individual and different kinetic stimulations can dramatically affect intracellular signaling dynamics to create distinct cell phenotypes (Fujita et al., 2010; Granados et al., 2017; Kubota et al., 2012; Muzzey et al., 2009; Shimizu et al., 2010; Sorre et al., 2014; Thiemicke et al., 2019; Twohig et al., 2019; Wang et al., 2012; Young et al., 2013). However, from these previous studies, it is not understood how parameter uncertainty, model predictions, and model identification quantitatively depend on the amount and type of experimental data.

Here we systematically explore how multiple, kinetically distinct inputs can activate signaling pathways to achieve diverse signaling responses, and we show that this diversity of input-output relationships is key to the identification of predictive models for complex biological pathways (Figure 1). To demonstrate the feasibility of this task, we infer several models from single-cell time-lapse microscopy data for cell signaling in the conserved High Osmolarity Glycerol (HOG/p38) pathway, a prototypical mitogen-activated protein

kinase (MAPK) pathway in the yeast *Saccharomyces cerevisiae* that is important for stress adaptation and cell survival (Figure 1A) (Cuadrado and Nebreda, 2010; Saito and Posas, 2012; Thiemicke et al., 2019). This eukaryotic model system includes the most relevant features of signaling networks, including a terminal signaling protein (Hog1) and a branched protein network that comprises membrane sensors, phosphorelays, kinases, phosphatases, autoregulation, and feedback and feedforward loops that are found in the majority of signaling pathways (Lim and Bruce Mayer, 2017). With this system, it has been previously demonstrated experimentally that changing the extracellular osmolyte concentrations over time results in distinct Hog1 activation dynamics as pathway response output (Figures 1B and 1C) (Ferrigno et al., 1998; Hersen et al., 2008; Mettetal et al., 2008; Mitchell et al., 2015; Thiemicke et al., 2019). Because of these attributes that are common in many signal transduction pathways in eukaryotic cells, we now seek to explore what general implications the diversity of multiple input-to-output dynamics can have on the possibility to identify predictive signaling models and the regulatory mechanisms that are sensitive to kinetic environmental perturbations.

RESULTS

Parametrizing Signaling Models with Experimental Data Enables Predictions of Pathway Responses upon Kinetic Stimulations

As the HOG model pathway combines universal signaling network features as outlined earlier, it serves as a blueprint to build predictive signaling models of varying complexity (Figures 1A–1E). Previous published models have limitations in that they are too simple and lack molecular detail (Hersen et al., 2008; Muzzey et al., 2009) or that they are too complex having too many parameters to estimate (Klipp et al., 2005). Furthermore, other models are too specific, and their complexity is difficult to adapt when seeking to identify predictive models from finite amounts of experimental data (Granados et al., 2017; Schaber et al., 2012; Zi et al., 2010). To circumvent the challenge of variable complexity, we specify a class of expandable network topologies outlined in Figures 1E and S1K. In this class, model nodes are defined based on branching points in the Hog1 pathway starting from the Hog1 kinase, and complexity of the pathway can be increased by separating nodes into sub-nodes (Figure 1E, left to right) (Transparent Methods). For example, the representative model in Figure 1E (middle) resembles a simplified branched signaling pathway consisting of four nodes, including one activating and one repressing sensor protein, constant basal regulators, and a negative feedback loop from the terminal kinase to an upstream signaling branch (Figures S1A). In the context of the HOG pathway, the node x_1 represents the SLN1 branch including the proteins Sln1, Ypd1, Ssk1, and Ssk2/Ssk22. The SLN1 branch utilizes a two-component phosphorelay mechanism to transmit its signal, with b_1 representing the constant deactivation of the SLN1 branch (Hohmann et al., 2007; Maeda et al., 1994). The node x_2 describes the SHO1 branch of the HOG pathway that utilizes protein kinases to relay its information. The SHO1 branch consists of the proteins Sho1, Msb2, Hkr1, Opy2, Cdc42, Ste20/Cla4, Ste11, and Ste50, with b_2 modeling the basal deactivation of the SHO1 branch (Tatebayashi et al., 2015). The SHO1 branch is also regulated by the Hog1 kinase through a feedback loop (Hao et al., 2007; O'Rourke and Herskowitz, 1998; Westfall and Thorner, 2006). The node x_3 represents an MAPKK such as Pbs2 that integrates information flow from two branches and has basal regulation (b_3) through phosphatases such as Ptc1/2/3. Last, x_4 represents a terminal kinase such as Hog1 that is activated by Pbs2. Hog1 is deactivated through phosphatases Ptc1/2/3 and Ptp2/3 (Mattison and Ota, 2000; Warmka et al., 2001; Young et al., 2002). Deactivation of Hog1 via constitutively active phosphatases is modeled as the act of basal deactivator b_4 on x_4.

We parametrized these representative biologically inspired models (Transparent Methods) by fitting them to experimental Hog1 nuclear localization data (Figures 1B and S1K–S1M). Using experimentally constrained parameters for each model, we predicted Hog1 signaling dynamics upon different kinetic stimulation profiles and evaluated each model's ability to predict independent experimental Hog1 dynamics. The model (Figure 1E, middle) and the parameter set (Table S1) resulting in the smallest prediction error was defined as the "true model" and the "true parameters," respectively. From this model, we simulate synthetic signaling data upon diverse kinetic stimulations for the remainder of this study. Using a known model for this task, rather than additional experiments, allows us to systematically and quantitatively establish how diverse kinetic stimulations impact model identifiability and predictive power in a controlled setting where ground truth knowledge is available to check performance.

Diverse Kinetic Cell Stimulations Result in Distinct Pathway Activation Dynamics

With a specified "true model," we can now rigorously explore diverse kinetic inputs to pathway dynamics (Figure 1G). We simulated 54 synthetic datasets (Figures 1H, and S2) under a wide range of physiologically

feasible and mutually independent kinetic stimulation profiles (see Transparent Methods) such that each of the 54 profiles stimulates the pathway to express a unique temporal behavior. Our simulated data (Figures 2 and S2) qualitatively and quantitatively capture the main characteristics of measured dynamics for Hog and other signaling pathways, including modulation of activation level, diversity of signaling dynamics, delayed onset of activation, variable time to reach maximum activation, perfect adaptation, and measurement error observed in experiments (Figures 1B and 1C). Each signaling dataset covers the same duration and sampling range and has the same amount of data. However, different datasets may constrain model parameters to different extents that, in turn, could lead to predictions of different accuracy. To compare the performance of kinetic stimulations, we also simulated signaling activation dynamics upon staircase, pulsatile, and sinusoidal stimulation inputs (Figures 1H, datasets 55–58, and S3).

Lack of Kinetic Stimulation Diversity Limits Model Prediction Power

To explore what effects different stimulations have on model predictive power, we fit the true model to many independent sets of simulated data with experimentally realistic noise (Transparent Methods). The results of model fit simultaneously for two steps of 0.2 and 0.3 M NaCl is shown in Figure 2A (red). After confirming that these fits had converged to maximize the likelihood of observing the training data (Figures S1G–S1J; Transparent Methods), we then predicted the remaining 54 datasets for steps as well as all other kinetics (blue) (Figure 2). Comparison of the fits and predictions to the corresponding training and testing data shows that the quality of predictions is nearly as good as fits for the *same* type of kinetics (Figures 2A and 2J, blue), but predictions become worse for *different* types of kinetics (Figures 2B–2F, 2G–2I, 2K, and 2L). This raises the question if the lack of predictability is due to the lack of data or due to limited kinetic diversity in the training data.

To address the possibility of having too little data, we fit the model to six-step (t^0) data simultaneously (Figure 3A, red), and we predicted the signaling dynamics upon all remaining kinetic stimulations (48 datasets). We compared model predictions of signaling dynamics for linear kinetic stimulations (t^1) or nonlinear kinetic stimulations (t^9) of different final concentrations to their corresponding synthetic data (Figure 3A, blue or green, respectively, compared to gray). After convergence, each set of model fits resulted in poor predictions for all datasets except for testing data collected using the same kinetic type as the training data. This observation was the same for subsequent training datasets with homogeneous input types (Figures S3A–S3C). Comparing how model predictability depends on the amount of training data of the same type illustrates that simply collecting *more* data of the same type does not automatically result in improved predictability (Figures 3B and S3A–S3C, right). Rather, the specific kinetics upon which the cells are stimulated may be of greater importance.

Diversified Kinetic Stimulations Better Constrain Model Parameters and Improve Model Predictions

To address the importance of kinetic diversity in training data, we fit signaling dynamics for different kinetic stimulations (t^0–t^7) of a given final concentration (Figure 3C, red), and we predicted the signaling dynamics for the remaining kinetic stimulations (Figure 3C, blue and green). Comparing model predictions of signaling dynamics for linear kinetic stimulations (t^1) or nonlinear kinetic stimulations (t^9) of several different final concentrations with their corresponding synthetic data (Figures 3C and S3D, blue or green, respectively, compared with gray) indicates that all the predictions are substantially improved and are nearly as good as the fits, whereas the amount of training data is still the same as in Figure 3A. Quantitatively comparing how model predictability depends on the amount of different types of training data illustrates that kinetically diverse training data substantially improve predictability under all test kinetics (Figure 3D, blue, yellow, or green quantified from testdata1, testdata2, or testdata3).

Our results indicate that a minimum of five diverse training datasets are sufficient to achieve average prediction errors within 75% of the standard deviation of data, and six diverse datasets result in average prediction errors within 51% of the standard deviation of the data. For a more stringent evaluation of generality and extensibility, we then challenged the various trained models with entirely different sets of novel alternating stimulations including staircase, pulsatile, or complex sinusoidal oscillatory inputs (testdata4) (Figures 3E–3G and S3E–S3H). After training using six steps (Figures 3A and S3I), six t^5 kinetics (Figure S3J), or six diverse kinetics (Figures 3C and S3K), we compared model predictions with their corresponding simulated data for four alternative stimulations (S3E–S3K, purple compared with gray). Finally, we fit each of the 11 different training datasets and predict the remaining data (Figure 3H). Each of the 11 different training

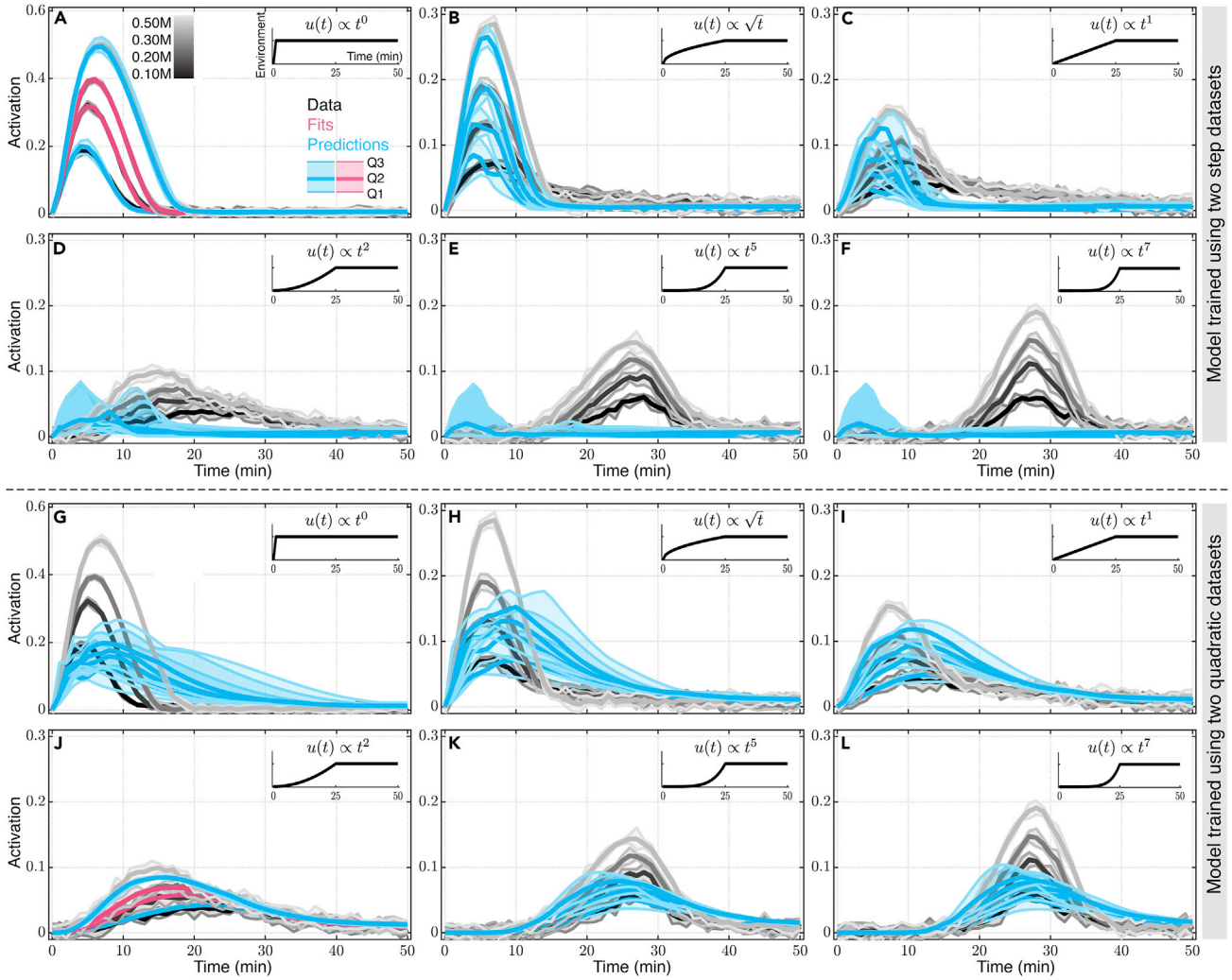

Figure 2. Models Trained Using Same Kinetic-Type Inputs Fail to Predict Pathway Response to Other Kinetics

(A–F) Models trained using step inputs fail to predict pathway response to kinetic stimulations. Gray lines show synthetic pathway activation dynamics over time at different kinetic inputs as indicated inside each panel: step (t^0, A), root ($\sqrt{t}$, B), linear (t^1, C), quadratic (t^2, D), quint (t^5, E), and heptic (t^7, F) input kinetics over time each to increasing final concentrations of 0.10, 0.20, 0.30, and 0.50 M. (A) Model fit simultaneously to steps of 0.2 and 0.3 M data are shown in red. (A–F) Predictions under all other conditions are shown in blue. Predictions in (E) and (F) of all four concentrations overlap. Thick lines and shaded areas show median and interquartile range out of 10 independent fits and their corresponding predictions, respectively. As shown as an inset in (A), the first, second, and third quartiles are used to plot shaded error bars where the thick line and upper and lower shaded areas represent Q2, (Q3-Q2), and (Q2-Q1), respectively. This convention is used throughout the article.

(G–L) Similar to (A–F), models trained using quadratic inputs fail to predict pathway response to other kinetics.

See also Figure S2.

datasets contains the same amount of data and fits equally well to its respective training data, but training using diverse kinetics led to far better predictions in comparison to any of the other sets of perturbations (Figure 3H). A comprehensive comparison of model predictions with all testdata under each of the 11 different training conditions is given in Video S1. A detailed analysis demonstrates that when using training data restricted to a single type, prediction errors increase as test data deviate away from kinetically similar training data (Figures 4A and S4A–S4I).

To better understand why multiple diverse kinetic stimulations result in better predictions and reduced predictions uncertainties, we next sought to analyze the effects of different training inputs on prediction errors (Figures 4B and S3A–S3D). By comparing predictions for an increasing number of training data, we find that prediction errors decrease with increase in the amount of training data regardless of the

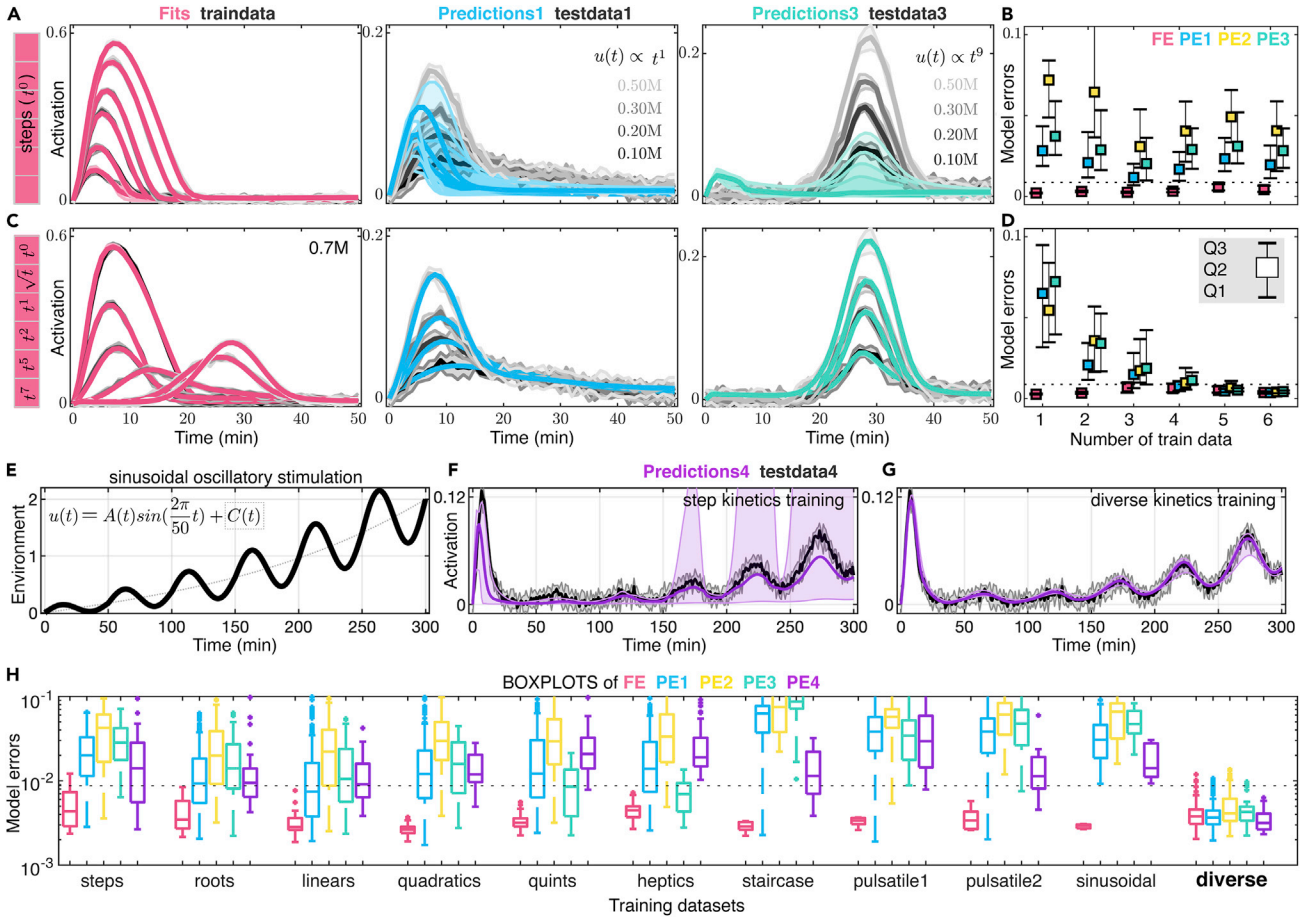

Figure 3. Kinetic Stimulation Improves Model Predictions

(A) Simultaneous fits (red) to six simulated step input response of different concentrations (gray) and subsequent model predictions of signaling dynamics upon different concentrations of linear input stimulations (predictions1 in blue, testdata1 in gray) or different concentrations of nonlinear inputs of the shape t^9 (predictions3 in green, testdata3 in gray).

(B) Box plots of fit and prediction errors when an increasing number of step inputs is used to train the model.

(C) Simultaneous fit (red) to six different kinetic input stimulations of the same final concentration (gray) and model predictions for different concentrations of linear input stimulations (predictions1 in blue, testdata1 in gray) or different concentrations of nonlinear input stimulations of the shape t^9 (predictions3 in green, testdata3 in gray). In (A and C), thick lines and shaded areas in gray show the mean and the standard deviation of synthetic data. Thick lines and shaded areas in red, blue, and green show median and interquartile range of 10 independent fits and their corresponding predictions, respectively.

(D) Box plots of fit and prediction errors when an increasing number of diverse kinetics (t^0 t^7) is used to train the model. For (B and D), squares and error bars show median and first and third quartiles, respectively. Horizontal dotted black line denotes the standard deviation of the simulated data. Fit or prediction errors (FE or PE1-PE4) are the mean absolute difference of the fit or predictions and their corresponding synthetic data over time (Transparent Methods). Fit error (FE) statistics are drawn from n_{train} datasets over 10 independent fits (10 × n_{train} errors) where n_{train} = 1,2, …6 is the number of datasets used to train the model. Similarly, PE1, PE2, and PE3 are drawn from prediction errors of testdata1 (36-n_{train} datasets over 10 independent fits), testdata2 (12 datasets over 10 independent fits), and testdata3 (6 datasets over 10 independent fits), respectively (Figure 1H).

(E–G) (E) Upon a sinusoidal oscillatory stimulation input (Figure S3H), model predictions (examples of P4 in purple) compared with testdata4 (gray) under (F) six steps versus (G) six diverse kinetics training.

(H) Full boxplots of fit (FE) and predictions errors (PE1, PE2, PE3, and PE4) compared with standard deviation of the synthetic data (horizontal dashed line) when six datasets of each kinetics (or equivalent) are used to train the model. Quantifications are from 10 independent fits for each condition. PE4 is prediction errors quantified from alternating stimulations that consist of staircase, pulsatile1, pulsatile2, and sinusoidal oscillatory inputs (Figures S3E–S3H). When either of the alternating stimulations is used as training data, PE4 is quantified over the other three alternating stimulations.

See also Figure S3 and Video S1.

training data type, but the prediction improvement is much faster when using diverse training data (Figure 4B). We applied both frequentist and Bayesian analyses to explore how variability in parameters and predictions arises from different experimental settings. For the frequentist analysis, we developed a Fisher Information Matrix (FIM) analysis framework to directly estimate the expected uncertainties of maximum

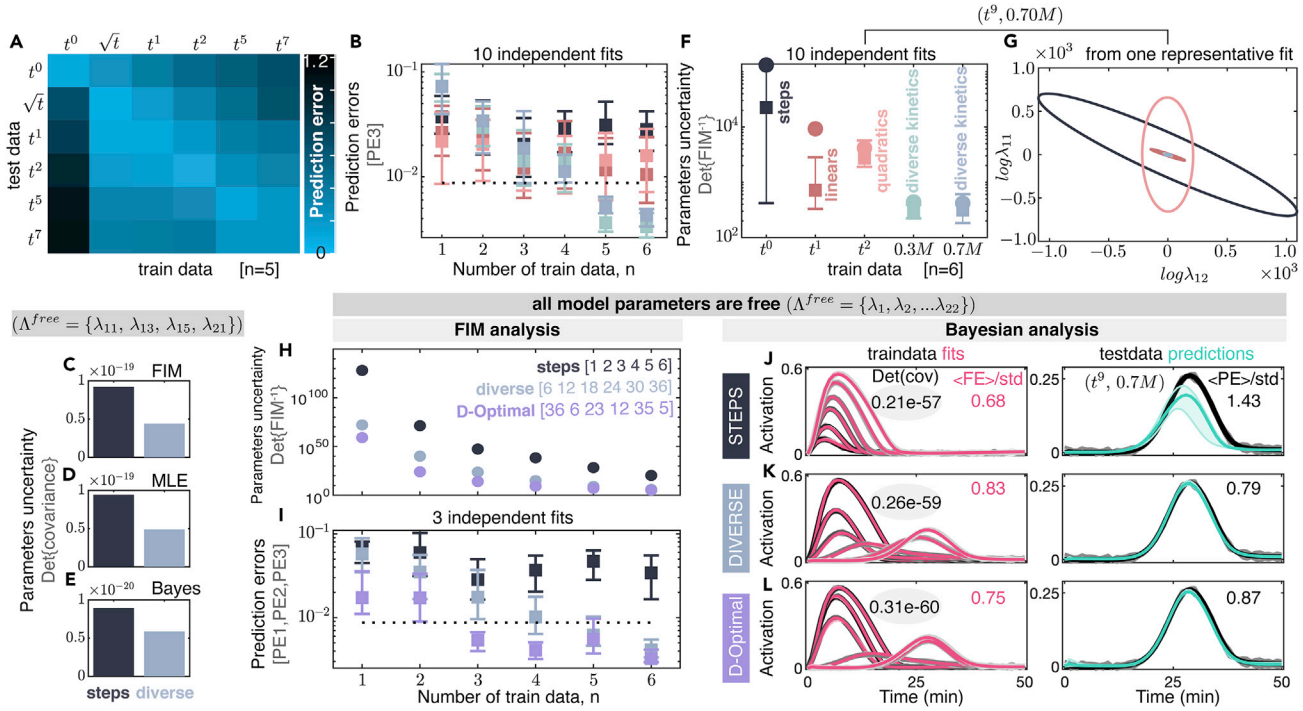

Figure 4. Kinetically Diverse Stimulations Constrain Model Parameters Substantially Better than Homogeneous Kinetic Types

(A) Comprehensive quantification of prediction errors of each kinetic stimulation type when five datasets of any given type is used to train the model (lighter colors denote smaller errors).

(B) Comparison of prediction errors (Predictions3) under increasing amounts of training data of the same kinetic type (e.g., step, linear, quadratic) or diverse kinetic types (0.3 and 0.7 M). Horizontal dotted black line denotes the standard deviation of the simulated data.

(C–E) Verification of FIM using MLEs. Under each of six step versus six diverse 0.7 M kinetics training, total model uncertainty is estimated by determinant of (C) FIM^{-1}, (D) covariance matrix of MLEs, and (E) covariance matrix of Bayesian posterior. Analyses in (C–E) are all performed with four free model parameters (λ11, λ13, λ15, λ21) (see Transparent Methods and Figures S4J and S4K).

(F) Parameter uncertainty of the model estimated as inverse of determinant of FIM (i.e., D-Optimality) when the model is fit to all six of each dataset.

(G) Ellipses are representative 95% confidence intervals for a representative pair of parameters estimated from FIM^{-1}. Colors correspond to the five different sets of experiments considered in (F).

(H) FIM optimal experimental design by minimizing the determinant of inverse FIM determines D-Optimal experiments for increasing number of datasets (n = 1,2, …6) among all possible combinations (36 choose n) (purple) compared with steps (black) or diverse 0.7 M (blue).

(I) Comparison of prediction errors (Predictions1, Predictions2, and Predictions3) under increasing amounts of training data of the steps, diverse 0.7 M, and D-Optimal experiments. Results are from three independent model fits and their corresponding predictions. Horizontal dotted black line denotes average standard deviation of the simulated data.

(J–L) Bayesian analysis to quantify model parameters posterior and predictions under different kinetics. Under (J) six steps, (K) six diverse 0.7 M, and (L) six D-Optimal training kinetics, model fits (red) and predictions (green) for 100 parameters sets sampled from Bayesian posterior are compared with their corresponding training and test data (gray). Results are from multiple independent chains (steps 3, diverse 3, and D-Optimal 7 chains) (see Transparent Methods). The values for the determinant of covariance of posterior (average over all independent chains), average fit errors (<FE>), and average prediction errors (<PE>) are given for each condition. The <FE> and <PE > quantifications are from 100 samples from posteriors of each independent chain. FE are from six training datasets; PE are from the remaining 52 test datasets (Figure 1H).

See also Figure S4.

likelihood estimations (MLE) when performing multiple independent replicas of the same experiment designs (Apgar et al., 2010; Fox and Munsky, 2019; Hagen et al., 2013; Komorowski et al., 2011) (Transparent Methods). We verified the FIM computation by performing MLE parameter searches for 1,000 simulated datasets per experiment design (Transparent Methods), and we found that 95% confidence intervals of MLE pairwise parameters match their 95% confidence intervals predicted by the FIM analysis (Figures 4C, 4D, S4J, and S4K). The verified FIM analysis shows that MLE estimates will have the least uncertainty when trained with diverse kinetic profiles when compared with homogeneous profiles (compare ellipses in Figures S4K and S4J, respectively). This improvement is explained by the fact that different kinetic profiles constrain different combinations of parameters resulting in different parameters uncertainties (Figures 4F and S4L–S4O), as shown for a specific pair of parameters (λ_{11},λ_{12}) that defines the regulation of the

terminal kinase through the activity of phosphatases (Figure 4G). Next, we employed a complementary Bayesian analysis to quantify the posterior uncertainty of parameters given a single set of training data (see Transparent Methods). In agreement with the frequentist analysis, we found that posteriors for homogeneous inputs were much broader than those found for the diverse input signals (Figure 4E).

Because the frequentist FIM analysis requires no data generation or fitting, it is many orders of magnitude more computationally efficient than the Bayesian analysis. Using the verified FIM to estimate the expected uncertainty for a given combination of input kinetics, we could next explore all possible combinations (36 choose n) for up to n kinetic inputs (2,391,495 total). Through this exhaustive search, we found that the D-Optimal (i.e., the set of experiments expected to minimize the determinant of FIM^{-1}) combination of $n = 6$ kinetic inputs was a diverse combination composed of inputs of two steps to 0.5 and 0.7 M (t^0), one root to 0.7 M ($\sqrt{t}$), one quadratic to 0.5 M (t^2), and two heptics to 0.5 and 0.7 M (t^7). This optimal experiment further reduces total parameter uncertainty compared with steps or the original diverse kinetics (Figure 4H). Comparing the determinants of covariance of the posterior (Det(cov)) for all parameters using the Bayesian approach, we find that the posterior for the FIM D-Optimal inputs was tighter when compared with diverse and homogeneous step input signals (compare Det(cov) in Figures 4J–4L).

We next applied these frequentist and Bayesian perspectives to ask how parameter uncertainty affects prediction accuracy. To answer this question from the frequentist perspective (i.e., how sensitive are predictions to the spread of MLE-based estimations corresponding to different replicas of the same experiment), we sampled parameter sets from a multivariate distribution centered at the true parameters and distributed with a covariance matrix equal to the inverse FIM. To answer this question from the Bayesian perspective (i.e., how sensitive are predictions to parameter uncertainty after constraining to a single replica experiment), we used Monte Carlo to sample parameter sets from the posterior distribution (see Transparent Methods). In both cases, we found that predictions based upon models fit to the diverse data as well as the FIM D-Optimal design provided much tighter and more accurate estimates of behaviors in unseen testing conditions (Figures 4I–4L). Our results indicate that six-step training datasets achieve an average prediction error within 143% of the standard deviation of data. In comparison, six diverse and six D-Optimal datasets result in average prediction errors within 79% and 87% of the standard deviation of the data (compare <PE>/std in Figures 4J–4L). We find that with the optimally designed experiments, a combination of three diverse experiments (comprised of one step (t^0), one quadratic (t^2), and one heptic (t^7) input), constrain the parameters sufficiently well to make predictions within 70% of the standard deviation of the data (Figure 4I). For clarity, results in Figure 4I are obtained using the frequentist approach while those in Figures 4J–4L are obtained using the Bayesian approach.

These results indicate that signaling models built based on one type of kinetic stimulations may be predictive under different intensities of that same kinetic input, but they are likely to fail to predict pathway responses upon other types of kinetic stimulations. This is important to consider because most computational models to date are often parametrized with measurements performed under constant stimulation profiles (Hao and O'Shea, 2012; Shaw et al., 2019). We find that training the model simultaneously with diverse kinetics constrains parameters better and improves predictions substantially.

Diverse Kinetic Stimulations Improve Identification of Model Structures

Next, we examined how kinetically different cell stimulations affect model structure identifiability (e.g., the number and mechanisms of interacting signaling proteins), and we sought to elucidate the contribution of specific signaling proteins to overall dynamic signaling responses. Figures 5 and S5 show fits (red) and predictions (blue, yellow, green, and purple) of five models with varying complexity to six different signaling response dynamics. This analysis is performed using datasets that are simulated from model M3. Simpler models were built by removing one or two regulatory elements from M3 to form M2 or M1, respectively, to simulate two mutants of the true model where the corresponding kinase activities are removed resulting in loss of feedback regulations (Figures S5A–S5C). A more complex model was built by adding two extra regulation elements to the true model, which could represent unknown regulatory elements yet to be discovered such as feedbacks from the terminal kinase to the upstream kinases (Figure S5D, model M4) (Suzuki et al., 2020). Finally, another complex model is generated by adding an entirely new signaling branch consisting of a third sensor node and introducing three additional regulatory elements to the true model that could correspond to SHO1 sub-branches in the HOG pathway (Figure S5E, model M5) (Tatebayashi et al., 2015). As expected, the simplest model cannot fit all data simultaneously (Figures 5A, S5A, and S5B, red), whereas the true model and the more complex models both fit well to the simulated data

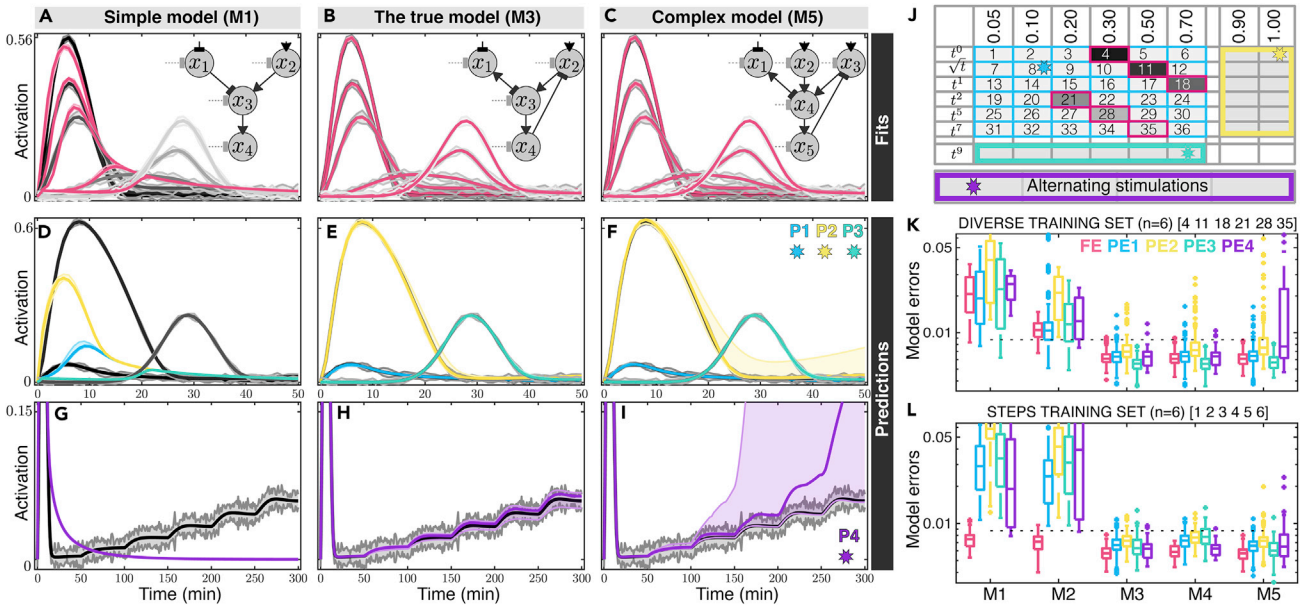

Figure 5. Kinetically Diverse Stimulation Profiles Enable Unprecedented Model Predictions

(A–I) Predictions enable identification of the true model among models of increasing complexities. (A–C) Three models with increasing complexity from left to right (M1 in A, M3 in B, and M5 in C) each are trained with six diverse kinetics datasets that are simulated from M3 (see Transparent Methods). Model fits are shown in red and compared with training data in gray. (D–I) Model predictions (examples of Predictions1 in blue, Predictions2 in yellow, Predictions3 in green, and Predictions4 in purple) are compared with their corresponding test data (gray) indicated with stars in the table of train/test data in (J). Thick lines and shaded areas in gray show the means and the standard deviations of synthetic data, respectively. Thick lines and shaded areas in red, blue, yellow, green, and purple show 10, 50, and 90 percentiles out of independent MLE fits of each model and their corresponding predictions over time.

(J) An overview of sets of training and testing data that are used for fits and predictions. Red, blue, yellow, green, and purple squares indicate the datasets used in (K), and stars indicate predictions that are presented in (D–I). (K) Quantification (boxplots) of fit and prediction errors for five models of increasing complexity after training each model with six diverse kinetics (see Transparent Methods and Figure S5 for model definitions and further analysis). Horizontal dotted black line denotes the standard deviation of the simulated data. Fit errors (FE) statistics are drawn from six train datasets over multiple independent trainings. Similarly, PE1, PE2, PE3, and PE4 are drawn from prediction errors of testdata1 (30 datasets, blue in J), testdata2 (12 datasets, yellow in J), testdata3 (6 datasets, green in J), and testdata4 (4 datasets, purple in J with stimulation profiles given in Figures S3E–S3H), respectively, each collected over multiple independent fits. Predictions for M4 and M5 are all specifically collected from MLEs that have objective of at least as low as that of converged M3 MLEs.

(L) Quantification of fit and prediction errors for five models of increasing complexity after training each model with six step kinetics. See also Figure S5.

(Figures 5B, 5C, and S5C–S5E, red). In each case, multiple MLEs were performed and models were then used to make four sets of predictions (Figures 5D–5I, blue, green, yellow, purple) (see Transparent Methods). As expected, the simple model does not predict well (Figures 5D and 5G), whereas the medium and complex model predictions are consistent with the true responses, but with an increasing level of prediction uncertainties (Figures 5E, 5F, 5H, and 5I).

We next performed systematic cross-validation of fits to specific input-output responses and prediction validation analyses using other datasets to explore how identification of a predictive model structure (e.g., selecting among models M1 to M5) depends on the specific types of training and validation data (Figures 5J–5L, S5F, and S5G). In all cases, as the model complexity increases from M1 to M5, the fits to training data improve monotonically (Figures 5K and 5L, S5F, and S5G, red), but the validation errors should reach a minimum when using the model structure that is most predictive given the available data (Figures 5K and 5L, S5F, and S5G, non-red markers). When training data consist of steps, simpler models (M1 and M2) fit well to the simulated data, therefore it is not possible to distinguish the true model using only steps data (Figure 5L). By quantifying predictions of each model upon all kinetic inputs (Figure 5J), it is possible on average to identify the true model (M3), but the certainty of structure identification depends heavily on the type of validation data (compare different colors in Figure 5L). In comparison, similar to diverse training data (Figure 5K), when using optimal experiments suggested by the FIM analysis, the over-simplified models fit less well to training data (Figures S5F and S5G), and validation data allowed for more certain selection of the true model. These results demonstrate that different kinetic cell stimulations can improve predictability in the process of complex model structure identification.

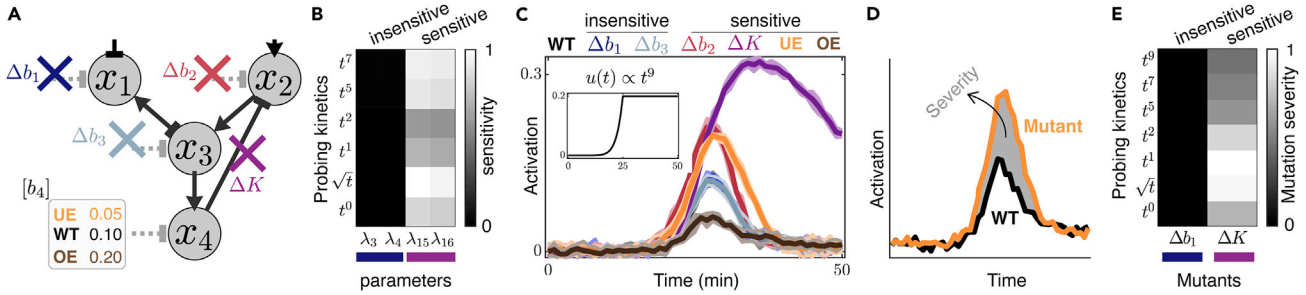

Figure 6. Kinetically Diverse Stimulations Elucidate Dynamic Effects of Mutants

Training the WT true model (M3 in Figure 5B) on its signaling dynamics upon diverse kinetics (red in Figure 5J) reveals insights into the response of several mutated models under all tested kinetic inputs. (A) The six mutants of the WT model correspond to deletions of basal regulators (e.g., phosphatases) on x_1 (Δb_1, blue), x_2 (Δb_2, red), or x_3 (Δb_3, teal); removal of the kinase activity (e.g., kinase dead or inhibited MAPK) of x_4 (ΔK, purple); and under- or overexpressing b_4 (e.g. phosphatase) that regulates x_4 (UE in orange and OE in brown). (B) Sensitivity analysis of WT model with respect to model parameters around their best value from the fits predicts insensitive (e.g., λ_3 and λ_4 corresponding to Δb_1) and sensitive (λ_{15} and λ_{16} corresponding to ΔK) mutants (see Figure S6). (C) Comparing the activation dynamics of mutants (simulated using Λ^0 in Table S1) with WT under a representative kinetic input (t^9 to 0.2 M, inset). Thick line and shaded area (colors) show the mean and the standard deviation of synthetic data for the corresponding strains. (D) Mutation severity, defined as the difference in activation dynamics of a mutant from that of the WT (Transparent Methods). (E) Mutation severity is shown for two representative mutant strains, Δb_1 (insensitive) and ΔK (sensitive) over all kinetic types summed over all their final concentrations. See also Figure S6.

Diverse Kinetic Stimulations Improve Predictions of Mutant Responses

Finally, we examined how diverse kinetic stimulations affect predictive performance for other *in silico* biologically realistic mutations to specific signaling proteins in signal transduction pathways (Figures 6A and S6) (Hohmann et al., 2007; Mattison and Ota, 2000; O'Rourke and Herskowitz, 1998; Westfall and Thorner, 2006; Young et al., 2002). Sensitivity analysis of the wild-type (WT) model that was trained with diverse kinetics allowed us to categorize model parameters into two main groups of insensitive (sensitivity = 0) and sensitive (sensitivity = 1) parameters that we then use to predict putative mutations (Figures 6A, 6B, and S6). To determine whether diverse kinetic cell stimulations can identify biological mechanisms, we computationally introduced six mutations in our true model (Transparent Methods). These include three knockout mutants that remove basal deactivators on x_1 (Δb_1, blue cross), x_2 (Δb_2, red cross), or x_3 (Δb_3, teal cross). Mutants Δb_1 and Δb_2 can be interpreted as removing the constitutive deactivation of SLN1 or SHO1 branches, respectively, which could change the half-life of their active states. Mutant Δb_3 could represent regulation of Pbs2 through deletion of Ptc1/2/3 phosphatases. The node x_4 can be mutated by removing kinase activity of x_4 (ΔK, purple cross, e.g., kinase dead or kinase activity inhibited) and can be regulated through overexpression (b_4, OE, orange), and underexpression (b_4, UE, brown) of the basal deactivator on x_4 such as the Ptp2/3 phosphatases (Figure 6A).

We simulated corresponding synthetic pathway activations from all six mutants upon all 54 kinetic stimulations (Transparent Methods). Pathway activations upon a representative kinetic stimulation input of t^9 are shown for all six mutants compared with the WT in Figure 6C. To quantify the differences in signaling dynamics between normal and mutant cells, we define severity as the difference in the activation dynamics of a mutant compared with that of the WT (Figure 6D and Transparent Methods). We observed that pathway activation in some mutant strains shows no difference from WT under all kinetic inputs (Δb_1 and Δb_3, mutation "severity" = 0), whereas other mutants with non-zero severity (Δb_2, ΔK, UE, and OE) are different from WT (Figure 6C). Comparing the sensitivity with respect to specific parameters in the model (Figure 6B) with the severity of the corresponding mutants' effect on signaling dynamics (Figure 6E) highlights that sensitive parameters are indicators of how much specific mutations will affect signaling under different kinetics of specific types (Figure S6). Furthermore, constraining the parameters of WT model on its synthetic data under diverse kinetic stimulations enabled us to accurately predict the activation responses of all the six mutants over time under all 54 kinetic inputs tested (Figures 7 and S7). These results are quantitatively summarized in Figure 7E, showing that the prediction errors for simulated mutations are comparable to prediction errors of non-mutated WT cells.

DISCUSSION

Our experimental and simulation results demonstrate that different kinetic cell stimulations of a pathway give rise to distinct signaling activation dynamics (Figure 1). When compared with the same amount of

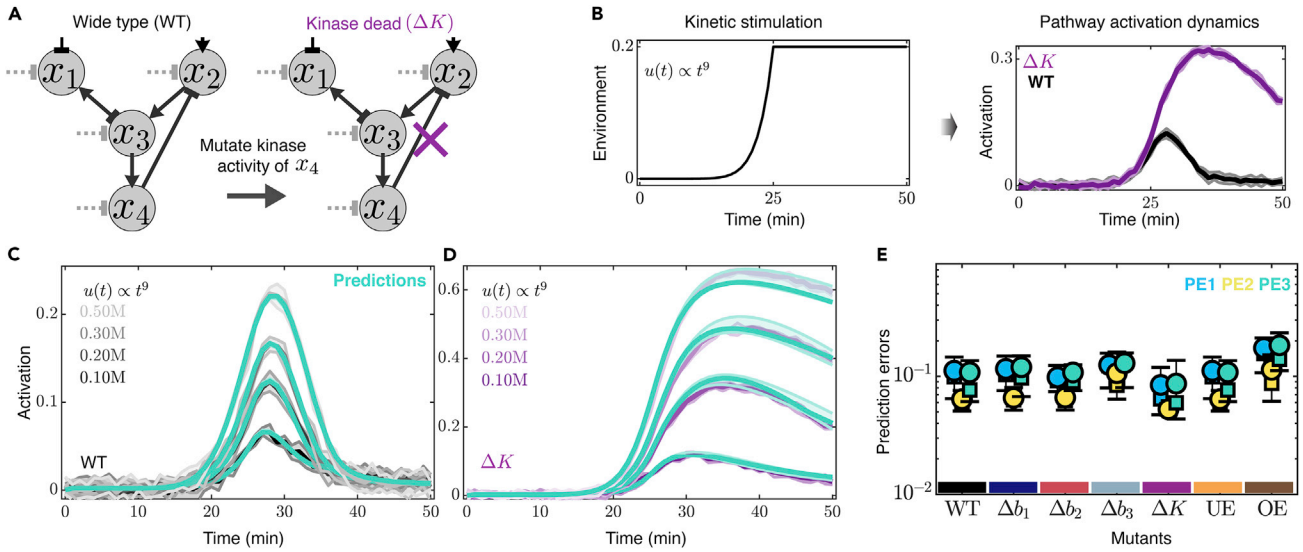

Figure 7. Kinetically Diverse Stimulations Enable to Predict Mutants' Response Dynamics

Training the WT true model on its signaling dynamics upon diverse kinetics enables predictions for the response of mutants upon all tested kinetic inputs.

(A) A mutant where the kinase activity of x_4 is eliminated (e.g., kinase dead or inhibited MAPK, purple cross) leads to a loss of feedback regulation from x_4 on x_2.

(B) Extracellular stimulation of the models results in elongated response adaptation in ΔK mutant compared with WT.

(C and D) Example pathway activation predictions (predictions3 in green) are compared with their corresponding synthetic data for WT (C, gray) and ΔK (D, purple) under representative t^9 kinetic inputs.

(E) Prediction errors (PE1, PE2, PE3) are quantified over all 54 kinetics (Figure 1H) for each of the six mutants (Figure 6A) compared with WT. These predictions are made using parameters constrained from five independent fits of WT model tarined on its signaling dynamics upon six diverse kinetics in Figure 5J. See also Figure S7.

any type of homogeneous kinetics, kinetically diverse cell stimulations perform much better to constrain complex model parameter sets and result in substantially reduced predictions errors (Figures 3 and 4). The FIM analysis approach provides a rigorous and clear mathematical interpretation of this effect. Specifically, the eigenvector of the FIM corresponding to the greatest eigenvalue indicates the parameter combination that is most likely to be accurately identified using a given kinetic stimulation (Figure S4O). By comparing eigenvectors corresponding to large FIM eigenvalues, it is easy to see which kinetic type may be most effective to constrain specific parameters of a complex regulatory network. Similarly, by examining eigenvectors corresponding to small FIM eigenvalues, it becomes apparent which parameter combinations cannot be precisely identified using a specific kinetic input. By choosing diverse and complementary input kinetics, such that the full parameter space is spanned by high-eigenvalue FIM eigenvectors from one or multiple kinetic inputs, it becomes possible to constrain the entire parameter set (Figures 4F, 4G, and S4L–S4O).

Better constrained parameters make it easier to identify predictive models of signal transduction (Figures 5 and S5). This also enables improved predictions of pathway activation dynamics for protein mutant strains upon kinetic stimulations (Figures 6, S6, and S7). To illustrate these predictions, we revisited the HOG pathway as an example (Figure 6). We predicted that mutations that alter the SLN1 branch (b_1) will not impact Hog1 signaling dynamics, which is consistent with previously published observation that changes in Ypd1 do not alter Hog1 signaling (Mukherji, 2010). Next we focused on the node x_2 that describes the SHO1 branch in which mutating b_2 could result in an increase or decrease in Hog1 signaling. We predicted that Δb_2 results in increased Hog1 signaling amplitude. In addition, the SHO1 branch can be altered in its activity by the feedback regulation from Hog1 kinase. In our model, we predicted that removing Hog1 kinase activity or inhibiting Hog1 kinase activity (ΔK) results in increased and prolonged Hog1 activation, which is consistent with previous published experimental work on small molecule inhibition of Hog1 activity (Muzzey et al., 2009; Westfall and Thorner, 2006). Next, we focused on the node x_3, which represents Pbs2. Our model predicted that deletions of individual phosphatases such as Ptc1/2/3 would not alter Hog1

signaling dynamics through changed Pbs2 activity (Δb_3) (Mapes and Ota, 2004; Warmka et al., 2001). Last, x_4 represents the terminal kinase Hog1 that can be deactivated through phosphatases Ptc1/2/3 and Ptp2/3 (b_4) (Martín et al., 2005; Murakami et al., 2008; Warmka et al., 2001; Young et al., 2002). The model predicted that changing the value of b_4 through over- or underexpression has a strong impact on Hog1 signaling intensity. The experimental observations of the effect of above-mentioned mutants on the HOG pathway dynamics under step profiles qualitatively aligns with our simulated data for all mutants validating our modeling approach for mutants (Figure 6) (O'Rourke and Herskowitz, 1998; Saito and Posas, 2012; Tatebayashi et al., 2015; Warmka et al., 2001). Using simulated data, we verified our mutant findings by quantitatively comparing predictions from each mutant to their corresponding synthetic data (Figure 7).

These results demonstrate that kinetic cell stimulations are ideally suited to discover novel regulatory interactions, reveal key functional proteins, identify predictive and biologically meaningful models, and help to gain novel insights to cell function or dysfunction. The potential for generality of kinetic stimulations is supported by emerging studies in many pathways and in different cell types. Examples are differential cellular responses upon step, pulsatile, or linear stimulations of EGF (Akt pathway, PC12 cells, Fujita et al., 2010), TGF-β (TGF-β pathways, myoblast progenitor C2C12 cell line, Sorre et al., 2014), cytokines IL-6 (STAT1/3, lymphocytes, Twohig et al., 2019) and TNF (NF-κB signaling, HeLa/neuroblastoma cells, Ashall et al., 2009; Mokashi et al., 2019), insulin (Akt/S6K pathway, rat hepatoma Fao cells, Kubota et al., 2012), H2O2 (Yap1 signaling, yeast cells (Goulev et al., 2017), or diacetyl in tetramisole hydrochloride (*C. elegans* AWA neurons, Rahi et al., 2017). We believe that implementing diverse kinetic stimulations may provide new opportunities in constraining complex model parameters in situations where experimental design methods based on instantaneous changes in the environment such as steps or pulses of varying heights or frequencies have not provided great success (Billings, 2013; Isermann and Münchhof, 2011). Given the complexity of signal transduction networks (Akhurst and Hata, 2012; Cildir et al., 2016; Hanahan and Weinberg, 2000; Hata and Chen, 2016; Hotamisligil and Davis, 2016) and their limited response bandwidths (Hersen et al., 2008), steps or pulsatile stimulations of even varying intensities or frequencies may not provide enough kinetics to efficiently probe the rich dynamics underlying these networks (Billings, 2013; Isermann and Münchhof, 2011). Our approach on the other hand is widely applicable to many biological pathways that respond to a kinetic cell stimulation with a dynamic signaling response, and our approach may have far-reaching implications for predicting pathway response upon specific mutations or drugs (Akhurst and Hata, 2012; Cildir et al., 2016; Hanahan and Weinberg, 2000; Handly et al., 2016; Hata and Chen, 2016; Hotamisligil and Davis, 2016; Janes and Lauffenburger, 2013; Rowland et al., 2011; Vanhaelen et al., 2017; Lim and Bruce Mayer, 2017). Being able to predict the pathway activation dynamics upon mutations or upon environmental changes may help design better drug treatment regimes. In addition, these results could benefit our understanding of human biology, particularly in areas such as optogenetics, gene regulatory networks, or synthetic biology, where predictive understanding of the system behavior with respect to extracellular kinetics or intercellular genetic perturbations is of immense interest (Aoki et al., 2019; Bashor et al., 2019; Gardner, 2013; Harrigan et al., 2018).

Limitations of the Study

The basic requirement for applying this framework to other systems is (1) that different environmental gradients can be generated, (2) that the pathway response changes over time, (3) that the pathway response time is homogeneous from cell to cell, and (4) that the central limit theorem is fulfilled in single cells.

RESOURCE AVAILABILITY

Lead Contact

Further information and requests for resources should be directed to and will be fulfilled by the Lead Contact, Gregor Neuert (gregor.neuert@vanderbilt.edu).

Materials Availability

This study did not generate new unique reagents.

Data and Code Availability

The datasets and code generated during this study are available at https://github.com/neuertlab/Jashnsaz_iScience_2020. The published article includes all datasets generated and analyzed during this study.

METHODS

All methods can be found in the accompanying Transparent Methods supplemental file.

SUPPLEMENTAL INFORMATION

Supplemental Information can be found online at https://doi.org/10.1016/j.isci.2020.101565.

ACKNOWLEDGMENTS

G.N. is supported by NIH, United States, DP2 GM11484901, NIH R01GM115892 and Vanderbilt Startup Funds. J.J.H. is supported by NIH, United States, T32DK101003 and NSF, United States, GRFP. Z.R.F. and B.M. are supported by NIH, United States, R35 GM124747. ZRF was also supported by the Agence Nationale de la Recherche, France, ANR-18-CE91-0002, CyberCircuits. The authors thank Amanda Johnson, Alexander Thiemicke, Benjamin Kesler, Rohit Venkat, Joseph Cleland, Eric Ron, and Stuart McKnight for comments on the manuscript. This study used resources at the Advanced Computing Center for Research and Education (ACCRE) at Vanderbilt University, Nashville, TN (NIH, United States, S10 Shared Instrumentation Grant 1S10OD023680-01 [Meiler]).

AUTHOR CONTRIBUTIONS

Conceptualization, G.N., B.M., H.J., and Z.R.F.; Methodology, G.N., B.M., H.J., and Z.R.F.; Software, G.N., B.M., H.J., Z.R.F., and J.J.H.; Validation, H.J. and Z.R.F.; Formal Analysis, H.J.; Investigation, H.J. and G.L.; Data Curation, H.J.; Writing – Original Draft, H.J., B.M., and G.N.; Writing – Review & Editing, H.J., B.M., G.N., Z.R.F., and J.J.H.; Visualization, H.J.; Supervision, G.N. and B.M.; Project Administration, G.N. and H.J., Funding Acquisition, G.N. and B.M.

DECLARATION OF INTERESTS

The authors declare that they have no conflict of interest.

Received: November 25, 2019
Revised: August 18, 2020
Accepted: September 11, 2020
Published: October 23, 2020

REFERENCES

Adler, M., and Alon, U. (2018). Fold-change detection in biological systems. Curr. Opin. Syst. Biol. *8*, 81–89.

Akhurst, R.J., and Hata, A. (2012). Targeting the TGFβ signalling pathway in disease. Nat. Rev. Drug Discov. *11*, 790–811.

Albeck, J.G., Mills, G.B., and Brugge, J.S. (2013). Frequency-modulated pulses of ERK activity transmit quantitative proliferation signals. Mol. Cell *49*, 249–261.

Aoki, S.K., Lillacci, G., Gupta, A., Baumschlager, A., Schweingruber, D., and Khammash, M. (2019). A universal biomolecular integral feedback controller for robust perfect adaptation. Nature *570*, 533–537.

Apgar, J.F., Toettcher, J.E., Endy, D., White, F.M., and Tidor, B. (2008). Stimulus design for model selection and validation in cell signaling. PLoS Comput. Biol. *4*, e30.

Apgar, J.F., Witmer, D.K., White, F.M., and Tidor, B. (2010). Sloppy models, parameter uncertainty, and the role of experimental design. Mol. Biosyst. *6*, 1890.

Ashall, L., Horton, C.A., Nelson, D.E., Paszek, P., Harper, C.V., Sillitoe, K., Ryan, S., Spiller, D.G., Unitt, J.F., Broomhead, D.S., et al. (2009). Pulsatile stimulation determines timing and specificity of NF-κB-dependent transcription. Science *324*, 242–246.

Bandara, S., Schlöder, J.P., Eils, R., Bock, H.G., and Meyer, T. (2009). Optimal experimental design for parameter estimation of a cell signaling model. PLoS Comput. Biol. *5*, e1000558.

Bashor, C.J., Patel, N., Choubey, S., Beyzavi, A., Kondev, J., Collins, J.J., and Khalil, A.S. (2019). Complex signal processing in synthetic gene circuits using cooperative regulatory assemblies. Science *364*, 593–597.

Billings, S.A. (2013). Nonlinear System Identification: NARMAX Methods in the Time, Frequency, and Spatio-Temporal Domains (John Wiley & Sons).

Briscoe, J., and Small, S. (2015). Morphogen rules: design principles of gradient-mediated embryo patterning. Dev *142*, 3996–4009.

Casey, F.P., Baird, D., Feng, Q., Gutenkunst, R.N., Waterfall, J.J., Myers, C.R., Brown, K.S., Cerione, R.A., and Sethna, J.P. (2006). Optimal Experimental Design in an EGFR Signaling and Down-Regulation Model. ArXiv. http://arxiv.org/abs/q-bio/0610024.

Cildir, G., Low, K.C., and Tergaonkar, V. (2016). Noncanonical NF-κB signaling in health and disease. Trends Mol. Med. *22*, 414–429.

Csete, M.E., and Doyle, J.C. (2002). Reverse engineering of biological complexity. Science *295*, 1664–1669.

Cuadrado, A., and Nebreda, A.R. (2010). Mechanisms and functions of p38 MAPK signalling. Biochem. J. *429*, 403–417.

Efremova, M., Vento-Tormo, R., Park, J.-E., Teichmann, S.A., and James, K.R. (2020). Immunology in the era of single-cell technologies. Annu. Rev. Immunol. *38*, 727–757.

Faller, D., Klingmüller, U., and Timmer, J. (2003). Simulation methods for optimal experimental design in systems biology. Simulation *79*, 717–725.

Ferrigno, P., Posas, F., Koepp, D., Saito, H., and Silver, P.A. (1998). Regulated nucleo/cytoplasmic exchange of HOG1 MAPK requires the importin β homologs NMD5 and XPO1. EMBO J. *17*, 5606–5614.

Fox, Z.R., and Munsky, B. (2019). The finite state projection based Fisher information matrix approach to estimate information and optimize

single-cell experiments. PLoS Comput. Biol. *15*, e1006365.

Fujita, K.A., Toyoshima, Y., Uda, S., Ozaki, Y.I., Kubota, H., and Kuroda, S. (2010). Decoupling of receptor and downstream signals in the Akt pathway by its low-pass filter characteristics. Sci. Signal. *3*, ra56.

Gardner, T.S. (2013). Synthetic biology: from hype to impact. Trends Biotechnol. *31*, 123–125.

Goulev, Y., Morlot, S., Matifas, A., Huang, B., Molin, M., Toledano, M.B., and Charvin, G. (2017). Nonlinear feedback drives homeostatic plasticity in H2O2 stress response. Elife *6*, e23971.

Granados, A.A., Crane, M.M., Montano-Gutierrez, L.F., Tanaka, R.J., Voliotis, M., and Swain, P.S. (2017). Distributing tasks via multiple input pathways increases cellular survival in stress. Elife *6*, e21415.

Groß, A., Kracher, B., Kraus, J.M., Kühlwein, S.D., Pfister, A.S., Wiese, S., Luckert, K., Pötz, O., Joos, T., Van Daele, D., et al. (2019). Representing dynamic biological networks with multi-scale probabilistic models. Commun. Biol. *2*, 1–12.

Hagen, D.R., White, J.K., and Tidor, B. (2013). Convergence in parameters and predictions using computational experimental design. Interf. Focus *3*, 20130008.

Hanahan, D., and Weinberg, R.A. (2000). The hallmarks of cancer. Cell *100*, 57–70.

Handly, L.N., Yao, J., and Wollman, R. (2016). Signal transduction at the single-cell level: approaches to study the dynamic nature of signaling networks. J. Mol. Biol. *428*, 3669–3682.

Hao, N., and O'Shea, E.K. (2012). Signal-dependent dynamics of transcription factor translocation controls gene expression. Nat. Struct. Mol. Biol. *19*, 31–39.

Hao, N., Behar, M., Parnell, S.C., Torres, M.P., Borchers, C.H., Elston, T.C., and Dohlman, H.G. (2007). A systems-biology analysis of feedback inhibition in the Sho1 osmotic-stress-response pathway. Curr. Biol. *17*, 659–667.

Harrigan, P., Madhani, H.D., and El-Samad, H. (2018). Real-time genetic compensation defines the dynamic demands of feedback control. Cell *175*, 877–886.e10.

Hata, A., and Chen, Y.G. (2016). TGF-β signaling from receptors to smads. Cold Spring Harb. Perspect. Biol. *8*, a022061.

Hersen, P., McClean, M.N., Mahadevan, L., and Ramanathan, S. (2008). Signal processing by the HOG MAP kinase pathway. Proc. Natl. Acad. Sci. U S A *105*, 7165–7170.

Hohmann, S., Krantz, M., and Nordlander, B. (2007). Yeast osmoregulation. Methods Enzymol. *428*, 29–45.

Hotamisligil, G.S., and Davis, R.J. (2016). Cell signaling and stress responses. Cold Spring Harb. Perspect. Biol. *8*, a006072.

Huang, Y., Liu, A.A., Lafon, B., Friedman, D., Dayan, M., Wang, X., Bikson, M., Doyle, W.K., Devinsky, O., and Parra, L.C. (2017). Measurements and models of electric fields in the in vivo human brain during transcranial electric stimulation. Elife *6*, e18834.

Isermann, R., and Münchhof, M. (2011). Identification of Dynamic Systems (Springer).

Janes, K.A., and Lauffenburger, D.A. (2013). Models of signalling networks-what cell biologists can gain from them and give to them. J. Cell Sci. *126*, 1913–1921.

Kinney, M.A., Vo, L.T., Frame, J.M., Barragan, J., Conway, A.J., Li, S., Wong, K.-K., Collins, J.J., Cahan, P., North, T.E., et al. (2019). A systems biology pipeline identifies regulatory networks for stem cell engineering. Nat. Biotechnol. *37*, 810–818.

Klipp, E., Nordlander, B., Krüger, R., Gennemark, P., and Hohmann, S. (2005). Integrative model of the response of yeast to osmotic shock. Nat. Biotechnol. *23*, 5.

Komorowski, M., Costa, M.J., Rand, D.A., and Stumpf, M.P.H. (2011). Sensitivity, robustness, and identifiability in stochastic chemical kinetics models. Proc. Natl. Acad. Sci. U S A *108*, 8645–8650.

Kubota, H., Noguchi, R., Toyoshima, Y., Ozaki, Y.I., Uda, S., Watanabe, K., Ogawa, W., and Kuroda, S. (2012). Temporal coding of insulin action through multiplexing of the AKT pathway. Mol. Cell *46*, 820–832.

Labib, M., and Kelley, S.O. (2020). Single-cell analysis targeting the proteome. Nat. Rev. Chem. *4*, 143–158.

Lim, W., and Bruce Mayer, T.P. (2017). Cell Signaling: Principles and Mechanisms (Garland Science, Taylor and Francis Group, LLC).

Maeda, T., Wurgler-Murphy, S.M., and Saito, H. (1994). A two-component system that regulates an osmosensing MAP kinase cascade in yeast. Nature *369*, 242–245.

Mapes, J., and Ota, I.M. (2004). Nbp2 targets the Ptc1-type 2C Ser/Thr phosphatase to the HOG MAPK pathway. EMBO J. *23*, 302–311.

Martín, H., Flández, M., Nombela, C., and Molina, M. (2005). Protein phosphatases in MAPK signalling: we keep learning from yeast. Mol. Microbiol. *58*, 6–16.

Mattison, C.P., and Ota, I.M. (2000). Two protein tyrosine phosphatases, Ptp2 and Ptp3, modulate the subcellular localization of the Hog1 MAP kinase in yeast. Genes Dev. *14*, 1229–1235.

Mettetal, J.T., Muzzey, D., Gómez-Uribe, C., van Oudenaarden, A., Bustamante, C., and van Oudenaarden, A. (2008). The frequency dependence of osmo-adaptation in Saccharomyces cerevisiae. Science *319*, 482–484.

Mitchell, A., Wei, P., and Lim, W.A. (2015). Oscillatory stress stimulation uncovers an Achilles' heel of the yeast MAPK signaling network. Science *350*, 1379–1383.

Mokashi, C.S., Schipper, D.L., Qasaimeh, M.A., and Lee, R.E.C. (2019). A System for analog control of cell culture dynamics to reveal capabilities of signaling networks. iScience *19*, 586–596.

Mukherji, S. (2010). Robustness and Tunability in Biological Networks (Massachusetts Institute of Technology).

Murakami, Y., Tatebayashi, K., and Saito, H. (2008). Two adjacent docking sites in the yeast Hog1 Mitogen-Activated Protein (MAP) Kinase differentially interact with the Pbs2 MAP Kinase Kinase and the Ptp2 protein tyrosine phosphatase. Mol. Cell. Biol. *28*, 2481–2494.

Muzzey, D., Gómez-Uribe, C.A., Mettetal, J.T., and van Oudenaarden, A. (2009). A systems-level analysis of perfect adaptation in yeast osmoregulation. Cell *138*, 160–171.

Oyler-Yaniv, A., Oyler-Yaniv, J., Whitlock, B.M., Liu, Z., Germain, R.N., Huse, M., Altan-Bonnet, G., and Krichevsky, O. (2017). A tunable diffusion-consumption mechanism of cytokine propagation enables plasticity in cell-to-cell communication in the immune system. Immunity *46*, 609–620.

O'Rourke, S.M., and Herskowitz, I. (1998). The Hog1 MAPK prevents cross talk between the HOG and pheromone response MAPK pathways in Saccharomyces cerevisiae. Genes Dev. *12*, 2874–2886.

Rahi, S.J., Larsch, J., Pecani, K., Katsov, A.Y., Mansouri, N., Tsaneva-Atanasova, K., Sontag, E.D., and Cross, F.R. (2017). Oscillatory stimuli differentiate adapting circuit topologies. Nat. Methods *14*, 1010–1016.

Romers, J., Thieme, S., Münzner, U., and Krantz, M. (2020). A scalable method for parameter-free simulation and validation of mechanistic cellular signal transduction network models. Npj Syst. Biol. Appl. *6*, 1–13.

Rowland, M., Peck, C., and Tucker, G. (2011). Physiologically-based pharmacokinetics in drug development and regulatory science. Annu. Rev. Pharmacol. Toxicol. *51*, 45–73.

Saito, H., and Posas, F. (2012). Response to hyperosmotic stress. Genetics *192*, 289–318.

Schaber, J., Baltanas, R., Bush, A., Klipp, E., and Colman-Lerner, A. (2012). Modelling reveals novel roles of two parallel signalling pathways and homeostatic feedbacks in yeast. Mol. Syst. Biol. *8*, 622.

Shaw, W.M., Yamauchi, H., Mead, J., Gowers, G.O.F., Bell, D.J., Öling, D., Larsson, N., Wigglesworth, M., Ladds, G., and Ellis, T. (2019). Engineering a model cell for rational tuning of GPCR signaling. Cell *177*, 782–796.e27.

Shimizu, T.S., Tu, Y., and Berg, H.C. (2010). A modular gradient-sensing network for chemotaxis in *Escherichia coli* revealed by responses to time-varying stimuli. Mol. Syst. Biol. *6*, 382.

Sorre, B., Warmflash, A., Brivanlou, A.H., and Siggia, E.D. (2014). Encoding of temporal signals by the TGF-β pathway and implications for embryonic patterning. Dev. Cell *30*, 334–342.

Steiner, R.A., Bremner, W.J., and Clifton, D.K. (1982). Regulation of luteinizing hormone pulse frequency and amplitude by testosterone in the adult male rat. Endocrinology *111*, 2055–2061.

Suzuki, S.K., Errede, B., Dohlman, H.G., and Elston, T.C. (2020). Model-driven experimental design identifies counter-acting feedback regulation in the osmotic stress response of yeast. BioRxiv, 051599, https://doi.org/10.1101/2020.04.20.051599.

Tatebayashi, K., Yamamoto, K., Nagoya, M., Takayama, T., Nishimura, A., Sakurai, M., Momma, T., and Saito, H. (2015). Osmosensing and scaffolding functions of the oligomeric four-transmembrane domain osmosensor Sho1. Nat. Commun. *6*, 6975.

Thiemicke, A., Jashnsaz, H., Li, G., and Neuert, G. (2019). Generating kinetic environments to study dynamic cellular processes in single cells. Sci. Rep. *9*, 10129.

Twohig, J.P., Cardus Figueras, A., Andrews, R., Wiede, F., Cossins, B.C., Derrac Soria, A., Lewis, M.J., Townsend, M.J., Millrine, D., Li, J., et al. (2019). Activation of naïve CD4+ T cells re-tunes STAT1 signaling to deliver unique cytokine responses in memory CD4+ T cells. Nat. Immunol. *20*, 458–470.

Vanhaelen, Q., Aliper, A.M., and Zhavoronkov, A. (2017). A comparative review of computational methods for pathway perturbation analysis: dynamical and topological perspectives. Mol. Biosyst. *13*, 1692–1704.

Wang, C.J., Bergmann, A., Lin, B., Kim, K., and Levchenko, A. (2012). Diverse sensitivity thresholds in dynamic signaling responses by social amoebae. Sci. Signal. *5*, ra17.

Warmka, J., Hanneman, J., Lee, J., Amin, D., and Ota, I. (2001). Ptc1, a type 2C Ser/Thr phosphatase, inactivates the HOG pathway by dephosphorylating the mitogen-activated protein kinase Hog1. Mol. Cell. Biol. *21*, 51–60.

Westfall, P.J., and Thorner, J. (2006). Analysis of mitogen-activated protein kinase signaling specificity in response to hyperosmotic stress: use of an analog-sensitive HOG1 allele. Eukaryot. Cell *5*, 1215–1228.

Young, C., Mapes, J., Hanneman, J., Al-Zarban, S., and Ota, I. (2002). Role of Ptc2 type 2C Ser/Thr phosphatase in yeast high-osmolarity glycerol pathway inactivation. Eukaryot. Cell *1*, 1032–1040.

Young, J.W., Locke, J.C.W., and Elowitz, M.B. (2013). Rate of environmental change determines stress response specificity. Proc. Natl. Acad. Sci. U S A *110*, 4140–4145.

Zhang, C., Tu, H.-L., Jia, G., Mukhtar, T., Taylor, V., Rzhetsky, A., and Tay, S. (2019). Ultra-multiplexed analysis of single-cell dynamics reveals logic rules in differentiation. Sci. Adv. *5*, eaav7959.

Zi, Z., Liebermeister, W., and Klipp, E. (2010). A quantitative study of the Hog1 MAPK Response to fluctuating osmotic stress in saccharomyces cerevisiae. PLoS One *5*, e9522.

iScience, Volume *23*

Supplemental Information

Diverse Cell Stimulation Kinetics Identify Predictive Signal Transduction Models

Hossein Jashnsaz, Zachary R. Fox, Jason J. Hughes, Guoliang Li, Brian Munsky, and Gregor Neuert

SUPPLEMENTAL FIGURES

SUPPLMENTAL TABLES

TRANSPARENT METHODS

SUPPLEMENTAL REFERENCES

SUPPLEMENTAL FIGURES

Figure S1

A **Signaling pathway**

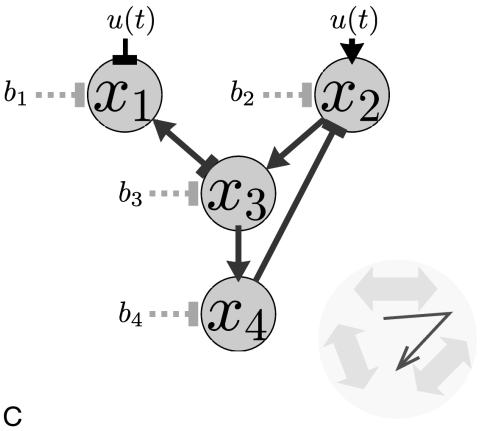

B **Matrix form of regulations**

Input $u(t)$ | Basal regulators | Internodes x_1 x_2 x_3 x_4

$$\begin{matrix} x_1 \\ x_2 \\ x_3 \\ x_4 \end{matrix} \begin{bmatrix} -1 \\ 1 \\ 0 \\ 0 \end{bmatrix} + \begin{bmatrix} -1 \\ -1 \\ -1 \\ -1 \end{bmatrix} + \begin{bmatrix} 0 & 0 & 1 & 0 \\ 0 & 0 & 0 & -1 \\ -1 & 1 & 0 & 0 \\ 0 & 0 & 1 & 0 \end{bmatrix}$$

D

$$x_3 = \frac{[X_3^*]}{[X_3^*] + [X_3]},$$

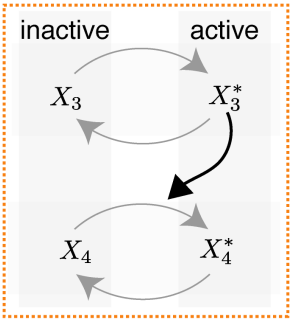

Michaelis–Menten equation

$$\frac{dx_4}{dt} = k_{cat}\, x_3 \frac{(1-x_4)}{K_{MM} + (1-x_4)}$$

C

Modeling the pathway as a **dynamic ODE system**.

$d\mathbf{x}/dt = \mathbf{f}(\mathbf{x}, \mathbf{b}, \mathbf{\Lambda}, u(t), t);\ \mathbf{x} = \{x_1(t), x_2(t), x_3(t), x_4(t)\},$

$$\frac{dx_1}{dt} = -\lambda_1 u(t)\frac{x_1}{\lambda_2 + x_1} - \lambda_3 b_1 \frac{x_1}{\lambda_4 + x_1} + \lambda_{13} x_3 \frac{(1-x_1)}{\lambda_{14} + (1-x_1)}$$
$$\frac{dx_2}{dt} = \lambda_5 u(t)\frac{(1-x_2)}{\lambda_6 + (1-x_2)} - \lambda_7 b_2 \frac{x_2}{\lambda_8 + x_2} - \lambda_{15} x_4 \frac{x_2}{\lambda_{16} + x_2}$$
$$\frac{dx_3}{dt} = -\lambda_9 b_3 \frac{x_3}{\lambda_{10} + x_3} - \lambda_{17} x_1 \frac{x_3}{\lambda_{18} + x_3} + \lambda_{19} x_2 \frac{(1-x_3)}{\lambda_{20} + (1-x_3)}$$
$$\frac{dx_4}{dt} = -\lambda_{11} b_4 \frac{x_4}{\lambda_{12} + x_4} + \lambda_{21} x_3 \frac{(1-x_4)}{\lambda_{22} + (1-x_4)}$$

E

$O_{sc}(t) = x_4(t) + c\xi(t); c = 0.020, \xi = \mathcal{N}(0,1)$, single cell trajectories
$O_{br}(t) =< O_{sc}(t) >_{sc}$, averaged single cell trajectories
$O(t) =< O_{br}(t) >_{br}$, population averages

$\mathbf{b} = \{b_1, b_2, b_3, b_4\}$
$= \{0.100, 0.100, 0.100, 0.100\}$, basal regulators
$\mathbf{x_0} = \{x_1(0), x_2(0), x_3(0), x_4(0)\}$
$= \{0.050, 0.050, 0.050, 0\}$, initial conditions
$\mathbf{\Lambda} = \{\lambda_1, \lambda_2, ...\lambda_{22}\}$, parameters

F **Optimization algorithm** {Model, Data}

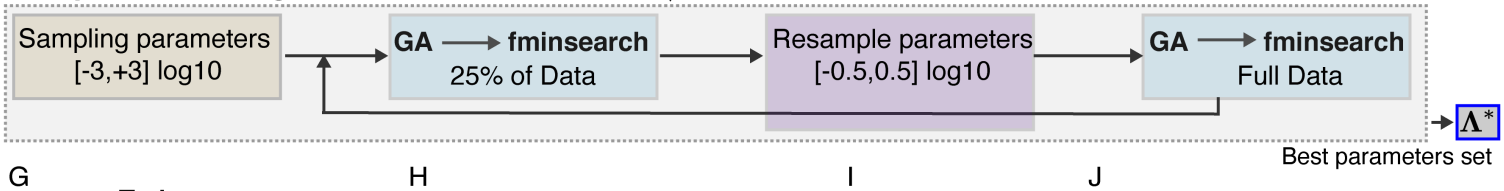

Best parameters set

G **Trains**

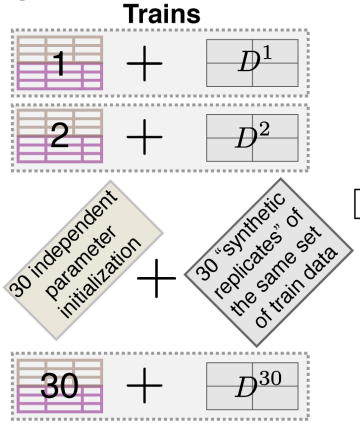

H **Fits**

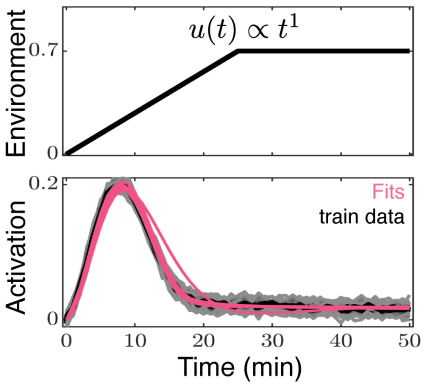

I **Best parameter sets**

J **Predictions**

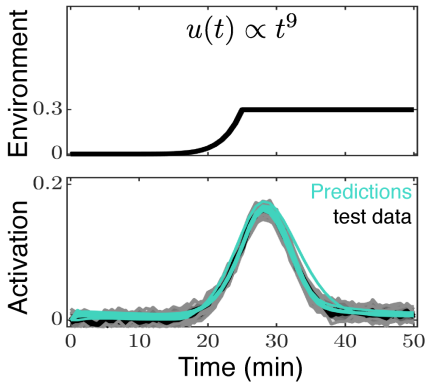

K

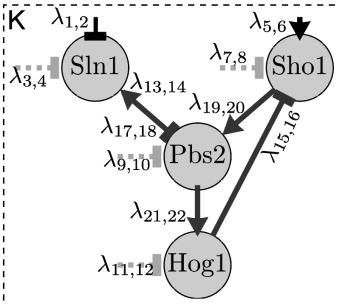

L **fits of model to 0.2M and 0.4M data individually**

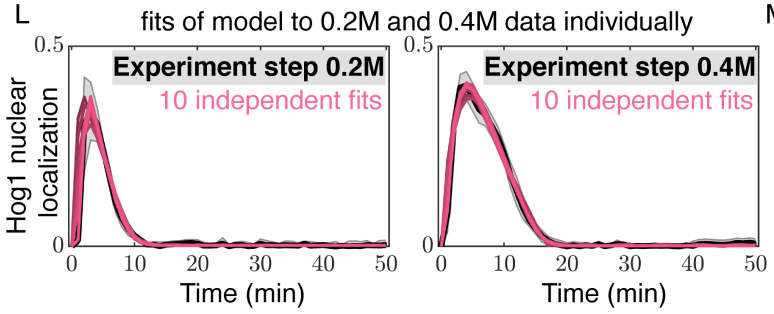

M **simultaneous fits**

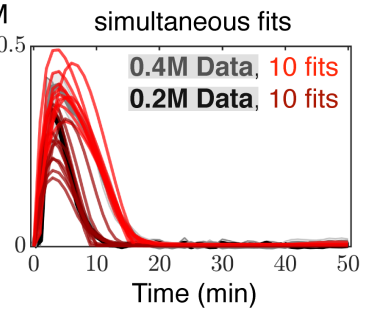

Figure S1. Signaling pathway, modeled as a dynamic ODE system, is parametrized using a custom optimization algorithm with Hog1 nuclear localization data. Related to Figure 1. (A) The signaling pathway is represented as a network topology diagram and is modeled as an enzymatic regulatory network described by a dynamic ordinary differential equations (ODE) system represented in (B) matrix form or (C) equation form. (D) A representative positive regulation in the model, where the active form of x_3 converts x_4 from its inactive to its active form (orange box in B and C) through a Michaelis-Menten function consisting of two parameters, the Michaelis-Menten constant (K_{MM}) and catalytic rate constant (k_{cat}). (E) The model is simulated with the initial and boundary conditions ($\boldsymbol{b}$ and $\boldsymbol{X_0}$) and Gaussian noise is added to the ODE solutions for $x_4(t)$ resulting in single cell pathway activation trajectories, $O_{sc}(t)$, under model parameters ($\boldsymbol{\Lambda^0}$) given in Table S1. Biological replicates are averaged from 10 simulated single cell trajectories. A signaling activation dynamic (e.g., each solid line and its shaded area in Figure S2) is calculated as the mean and the standard deviation of 5 simulated biological replicates. For convenience, we arrange the vector of parameters Λ such that even entries correspond to MM constants and odd entries correspond to catalytic rate constants. (F) Optimization algorithm. A combinatorial optimization algorithm using a customized Genetic Algorithm (GA) combined with fminsearch. The algorithm takes a model and a set of train data and returns a set of best parameter sets ($\boldsymbol{\Lambda^*}$) that best fit the training data. See Transparent Methods. (G-J) Fitting-prediction method. (G) For every condition presented in the manuscript, 30 independent fits are performed, each taking one of the 30 "synthetic replicates" of the simulated data along an independent random parameter initiation and resampling through the algorithm shown in (F). Each dotted box in (G) is equivalent to (F). (H) From resulted 30 fits, either 10 or 5 best converged optimizations (as indicated in each figure in the manuscript) are kept (each red line), and from the (I) resulted best parameter sets, (J) their corresponding predictions (each green line) are made upon any kinetic stimulation input (Transparent Methods). Here, the examples of fits (H, 10 red lines) and their corresponding predictions (J, 10 green lines) are shown from Figures 5A and 5C. In addition, at each best parameter set (I), upon each kinetic stimulation input, FIM (used to estimate parameter uncertainties) as well as sensitivity of the objective function with respect to parameters are also computed (Transparent Methods). This method was used for all results throughout this manuscript. (K,L) Ten independent fits (reds) of model in (K) to measured Hog1 nuclear localization data (black) upon steps of 0.2M (left) and 0.4M (right) applied to the cells at 0 min. Solid black line is mean and shaded area the standard deviations out of multiple biological replicates (Transparent Methods). (M) Ten best pairs of simultaneous fits to 0.2M and 0.4M Hog1 data out of 20 independent fits (dark and light reds) of model in (K). Constrained parameters of the model (K) under this fit that result in best predictions are given in Table S1 ($\boldsymbol{\Lambda^0}$). This parameter set is used to simulate all synthetic data for the WT (Figure S2) and mutants (Figure S7) upon kinetic stimuli.

Figure S2

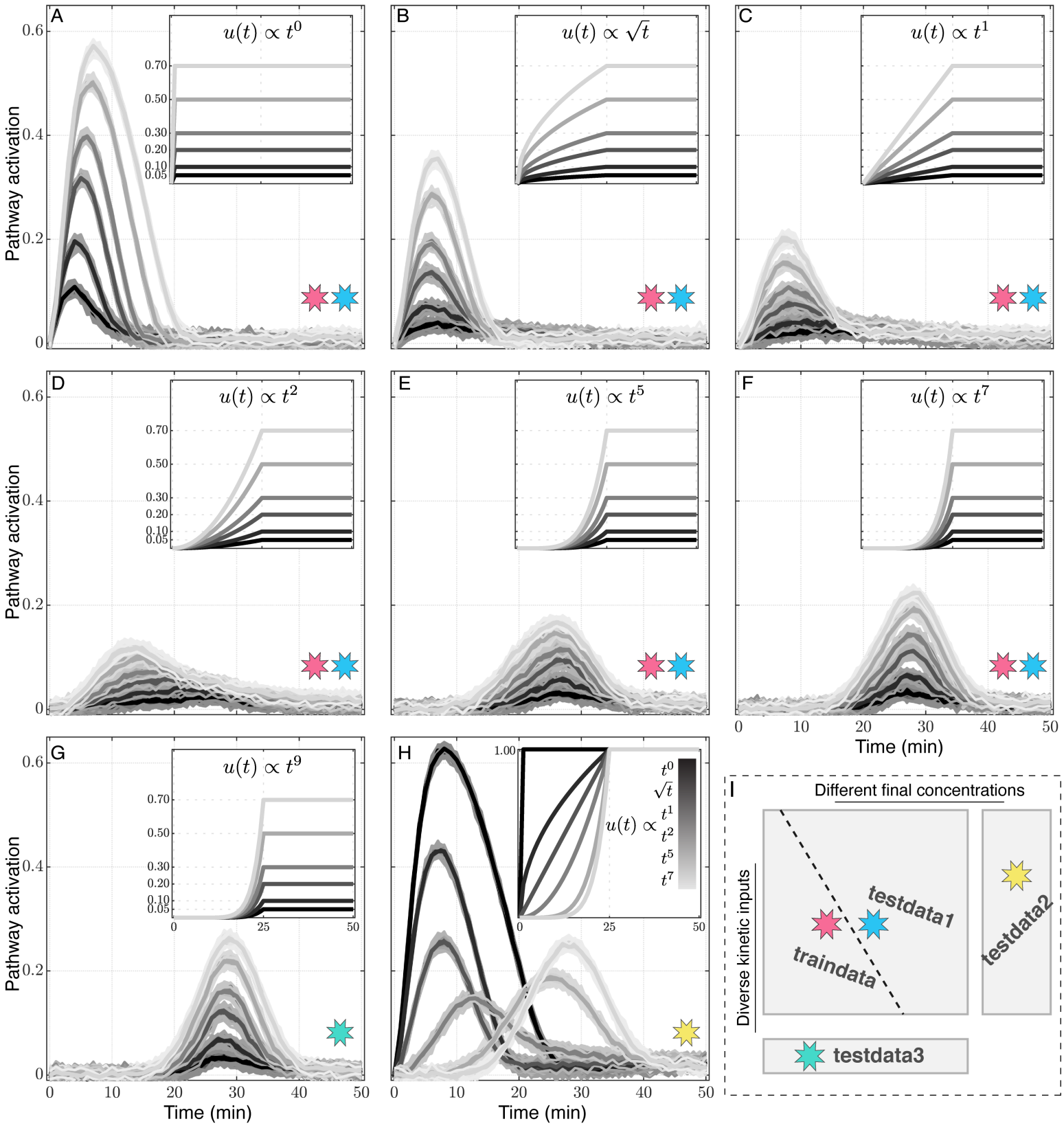
A
B
C
D
E
F
G
H
I
$u(t) \propto t^0$
$u(t) \propto \sqrt{t}$
$u(t) \propto t^1$
$u(t) \propto t^2$
$u(t) \propto t^5$
$u(t) \propto t^7$
$u(t) \propto t^9$
$u(t) \propto$
t^0
$\sqrt{t}$
t^1
t^2
t^5
t^7
Pathway activation
Time (min)
Different final concentrations
Diverse kinetic inputs
testdata1
testdata2
traindata
testdata3

Figure S2. Kinetic stimulations of signaling pathways result in dynamic pathway activation responses over a wide range of stimuli type and intensities. Related to Figures 1 and 2. Synthetic pathway responses simulated from WT model shown in Figure S1A upon diverse kinetic stimulations (inserts) as step (t^0, A), root ($\sqrt{t}$, B), linear (t^1, C), quadratic (t^2, D), quints (t^5, E), heptic (t^7, F), and nonic (t^9, G) functions over time each to final concentrations of 0.050, 0.10, 0.20, 0.30, 0.50, 0.70M. All kinetic stimulations start at 0 min, all except steps reach their final concentrations at 25 min, then keep constant from 25 min to 50 min (insets). (H) Data from diverse kinetic inputs (t^0, $\sqrt{t}$, t^1, t^2, t^5, t^7) all to 1.00M final concentration. 30 "synthetic replicates" (Transparent Methods) of each data is simulated under independent single cell noise (independent $\xi = \mathcal{N}(0,1)$ Gaussian noise). Solid black lines and shaded area represent the mean and the standard deviation of each data. (I) Red, blue, yellow, and green stars indicate each dataset belong to traindata, testdata1, testdata2, and testdata3, respectively (as in Figure 1H**),** to be used to train the model or to test model predictions.

Figure S3

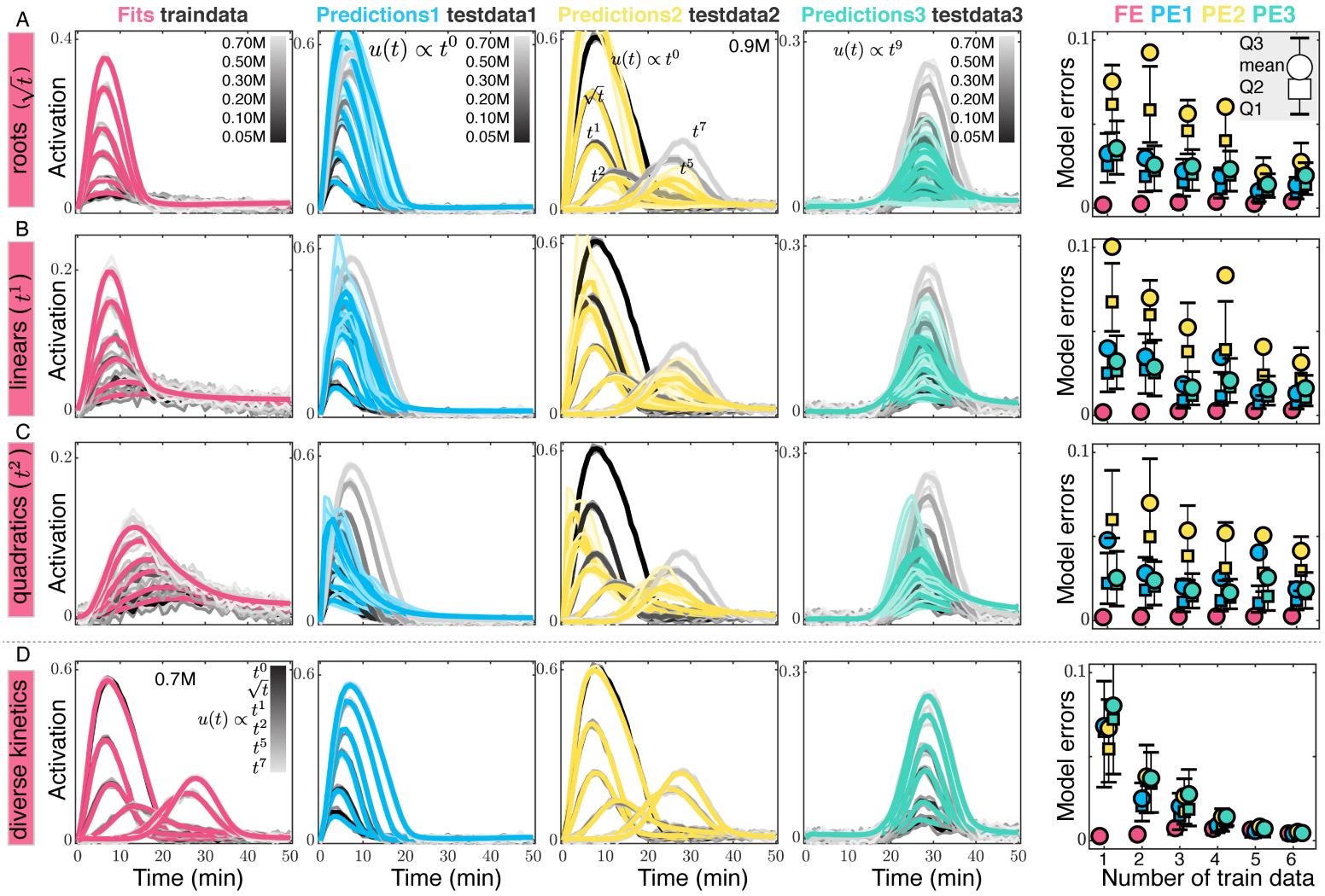
A
Fits traindata
Predictions1 testdata1
Predictions2 testdata2
Predictions3 testdata3
FE PE1 PE2 PE3
roots ($\sqrt{t}$)
linears (t^1)
quadratics (t^2)
diverse kinetics
Activation
Model errors
0.70M
0.50M
0.30M
0.20M
0.10M
0.05M
0.9M
$u(t) \propto t^0$
$u(t) \propto t^9$
Q3
mean
Q2
Q1
Time (min)
Number of train data

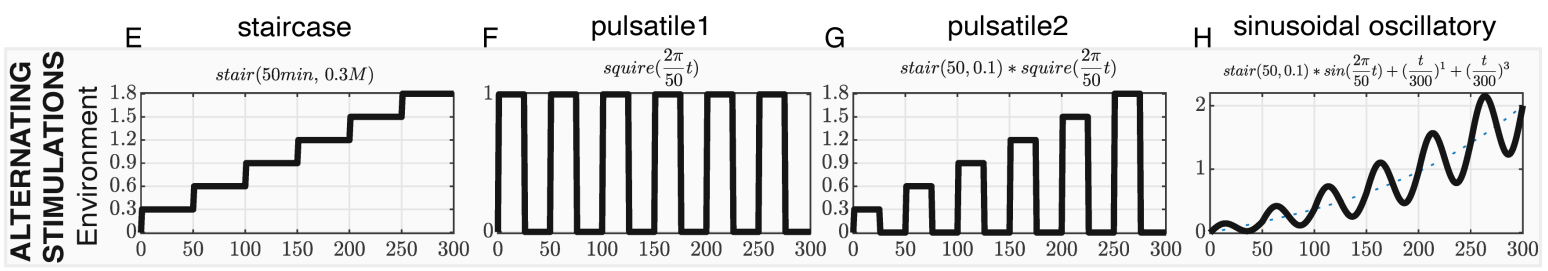
ALTERNATING STIMULATIONS
Environment
E staircase
$stair(50min,\ 0.3M)$
F pulsatile1
$squire(\frac{2\pi}{50}t)$
G pulsatile2
$stair(50,0.1) * squire(\frac{2\pi}{50}t)$
H sinusoidal oscillatory
$stair(50,0.1) * sin(\frac{2\pi}{50}t) + (\frac{t}{300})^1 + (\frac{t}{300})^3$

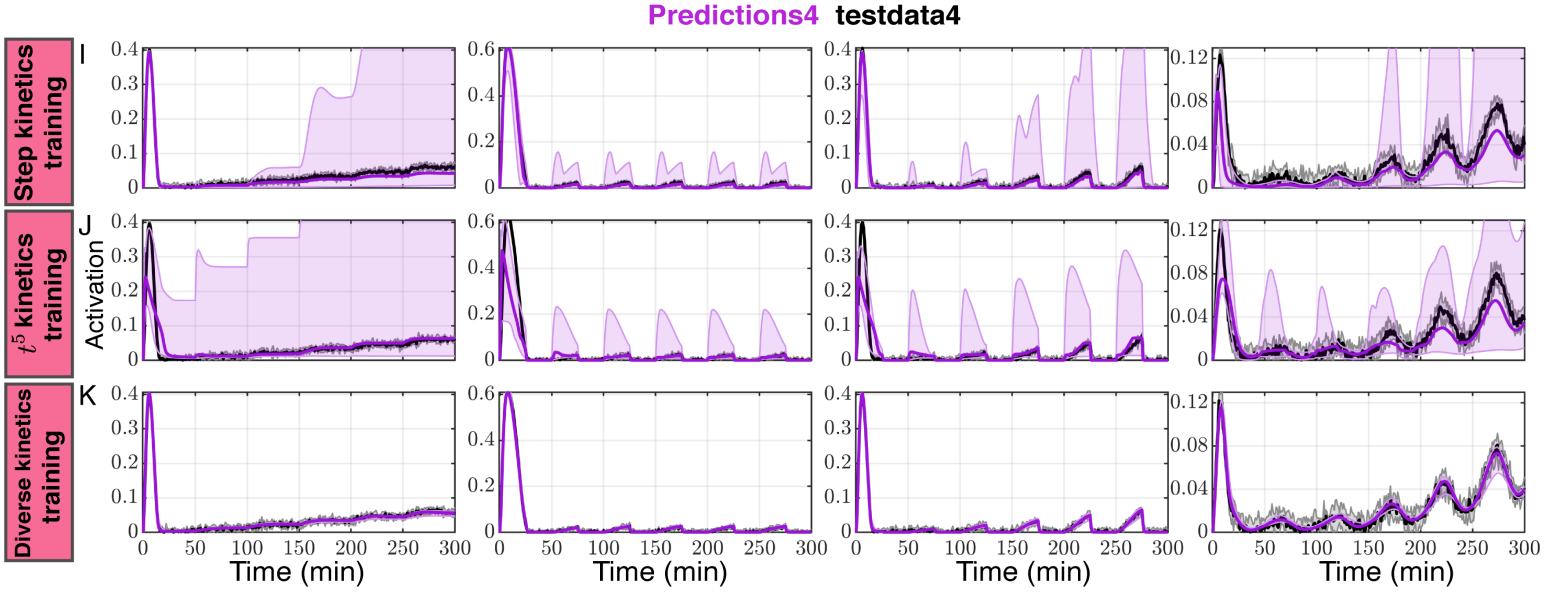
Predictions4 testdata4
Step kinetics training
t^5 kinetics training
Diverse kinetics training
I
J
K
Activation
Time (min)

Figure S3. Same kinetic type data fail to provide meaningful predictions regardless of amount of training data used. Related to Figure 3. (A) Model fits (red) simultaneously to all six root ($\sqrt{t}$) kinetics (gray) and predictions (blue, yellow, and green) are compared to their corresponding test data (gray): Predictions1 (blue) to testdata1 (step kinetics, gray), Predictions2 (yellow) to testdata2 (0.9M diverse kinetics, gray), and Predictions3 (green) to testdata3 (t^9 kinetics, gray). Right: quantifications of fit and prediction errors when increasing number of root data are used to train the model. (B) Similar to (A) this time instead of all six root ($\sqrt{t}$) kinetics data, all six linear (t^1) kinetics data are simultaneously used to train the model. Fits (red) are compared to their corresponding train data (gray). (C) All six quadratic (t^2) kinetics data are simultaneously used to train the model. (D) Six diverse kinetics data are simultaneously used to train the model. In (B-D) predictions (blue, yellow, and green) are compared to their corresponding testdata in gray (similar to A). Thick line and shaded area in gray show the mean and the standard deviation of synthetic pathway activation data. Thick line and shaded area in red, blue, yellow, and greens show median and interquartile range of 10 independent fits and their corresponding predictions, respectively. Quantifications of model errors are similar to Figure 3 (upon all 54 kinetics over 10 independent model fits for each condition). (E-H) Alternating stimulations including (E) a staircase, (F) pulse series of constant amplitude, (G) pulse series of increasing amplitude, and (H) a sinusoidal oscillatory stimulation input. (I-K) Model predictions of pathway activation upon each of the alternating stimulations under (I) six step kinetics training data, (J) six quint (t^5) kinetics training data, or (K) six diverse kinetics (0.70M) training data. Each of the alternating stimulations are independently used as training data in different experiments. For results see Movie S1 for a comprehensive presentation of model performance over all 58 kinetics under different training sets. In (I-K), shaded plots (purple) over time present 10, 50, and 90 percentiles out of 10 predictions4 corresponding to 10 independent fits of model for each condition.

Figure S4

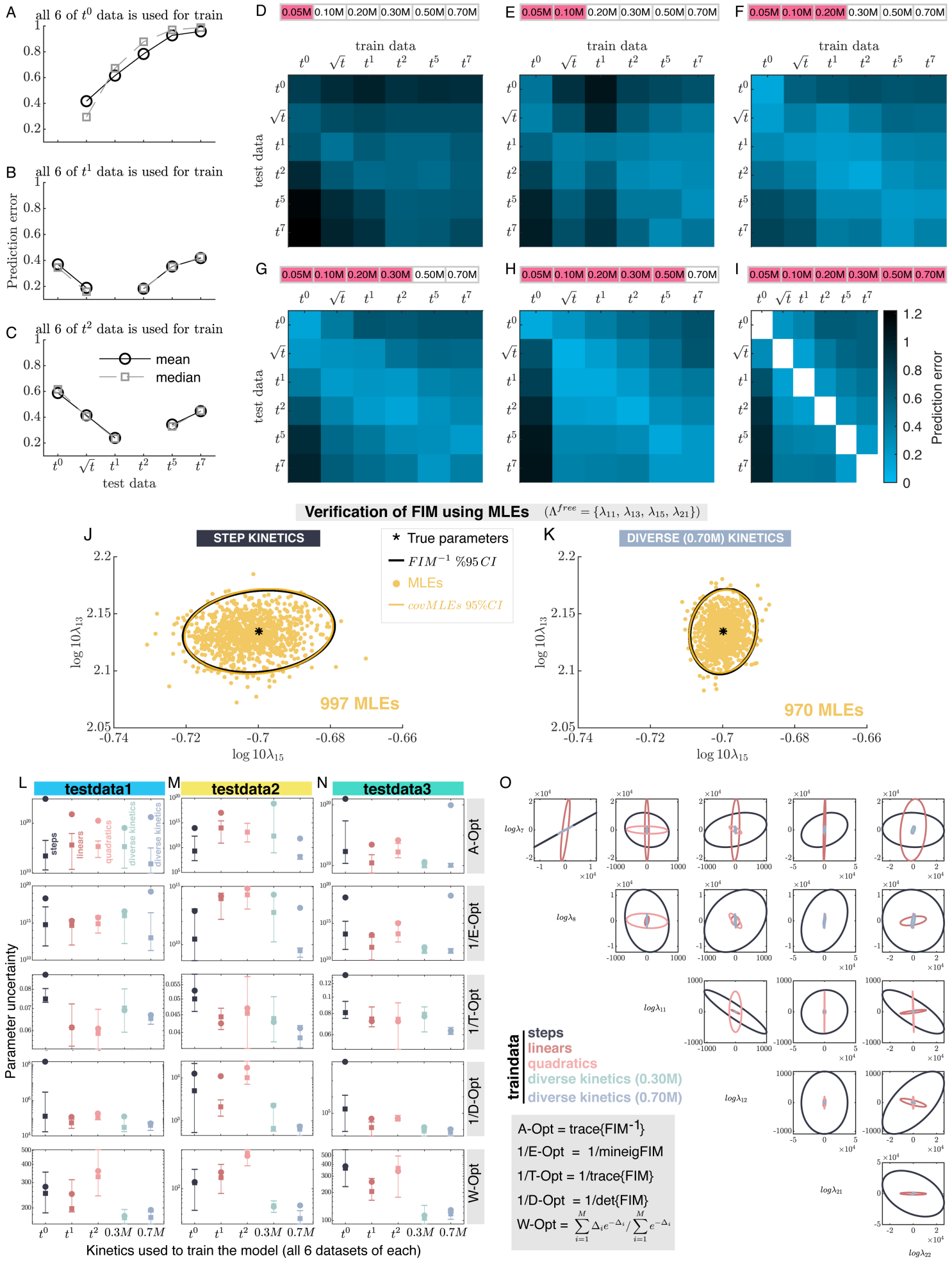
A
all 6 of t^0 data is used for train
B
all 6 of t^1 data is used for train
Prediction error
C
all 6 of t^2 data is used for train
mean
median
test data
D
E
F
train data
test data
0.05M 0.10M 0.20M 0.30M 0.50M 0.70M
G
H
I
Prediction error
Verification of FIM using MLEs ($\Lambda^{free} = \{\lambda_{11}, \lambda_{13}, \lambda_{15}, \lambda_{21}\}$)
J
STEP KINETICS
* True parameters
FIM^{-1} %95 CI
MLEs
covMLEs 95%CI
997 MLEs
K
DIVERSE (0.70M) KINETICS
970 MLEs
$\log 10\lambda_{13}$
$\log 10\lambda_{15}$
L
testdata1
M
testdata2
N
testdata3
steps
linears
quadratics
diverse kinetics
A-Opt
1/E-Opt
1/T-Opt
1/D-Opt
W-Opt
Parameter uncertainty
Kinetics used to train the model (all 6 datasets of each)
O
traindata
steps
linears
quadratics
diverse kinetics (0.30M)
diverse kinetics (0.70M)
A-Opt = trace{FIM^{-1}}
1/E-Opt = 1/mineigFIM
1/T-Opt = 1/trace{FIM}
1/D-Opt = 1/det{FIM}
W-Opt = $\sum_{i=1}^{M} \Delta_i e^{-\Delta_i} / \sum_{i=1}^{M} e^{-\Delta_i}$

Figure S4. Kinetically diverse stimulations constrain all model parameters while same kinetic type data are best effective on constraining some parameters but not others. Related to Figure 4. (A-I) Prediction errors increase by moving away from kinetically similar training data. (A-C) Quantification of prediction errors of each kinetic type when all six of steps (A), linears (B), or quadratics (C) are used to train the model. Kinetically similar data are best predictable, while by moving away from the kinetically similar train data predictions worsens quickly and dramatically. (D-I) Increasing the number of data (indicated with red boxes) from each type kinetics that is used to train the model (indicated on the x axis), and the predictions of each type of the kinetics (y axis) are quantified. Principal diagonals correspond to predicting test data that is kinetically similar to the train data (different final concentrations), which results in the best quality of predictions. All quantifications are from 10 independent fits for each condition. The prediction errors in (H, five training data) is as low as in (I, six training data) indicating that five training data are enough. This point is also reflected in the error quantifications given in Figure S3. (J-K) Verification of FIM using MLEs. Under (J) six step versus (K) six diverse 0.7M kinetics training, 95% confidence interval of model parameters uncertainty of pair (λ13, λ15) from FIM (black ellipses) is compared to that of MLEs (golden ellipses and dots). Each golden dot denotes one independent MLE (see *Transparent Methods*). (L-O) Using the same amount of data, kinetically diverse stimulations constrain model parameters substantially better than same kinetic types. Parameter uncertainty (magnitude) estimated via different optimalities of FIM under different kinetic stimulations. Under five different sets of traindata including six steps, six linears, six quadratics, six diverse kinetics of 0.30M or six diverse kinetics of 0.70M, FIM and FIM^{-1} are calculated upon all test data. The estimates of the model parameters uncertainty using each of A-Optimality, E-Optimality, T-Optimality, D-Optimality, and W-Optimality summed over for all of testdata1 (L), testdata2 (M), or testdata3 (N) kinetics and their boxplots out of 10 independent fits are shown for each condition. The fits are from Figures 3, S3 and S4I. W-Opt is defined as a weighted sum over the uncertainties (Δ^i) estimated by FIM^{-1} for individual parameters of the model (Transparent Methods). (O) Ellipses as eigenvectors representing 95% confidence intervals estimated from FIM^{-1} for few representative pairs of parameters. To clarify, similar results are obtained for all the model parameters. Under five different sets of traindata presented in L-O, as five different experiment designs, corresponding example ellipses are shown as indicated in the legend.

Figure S5

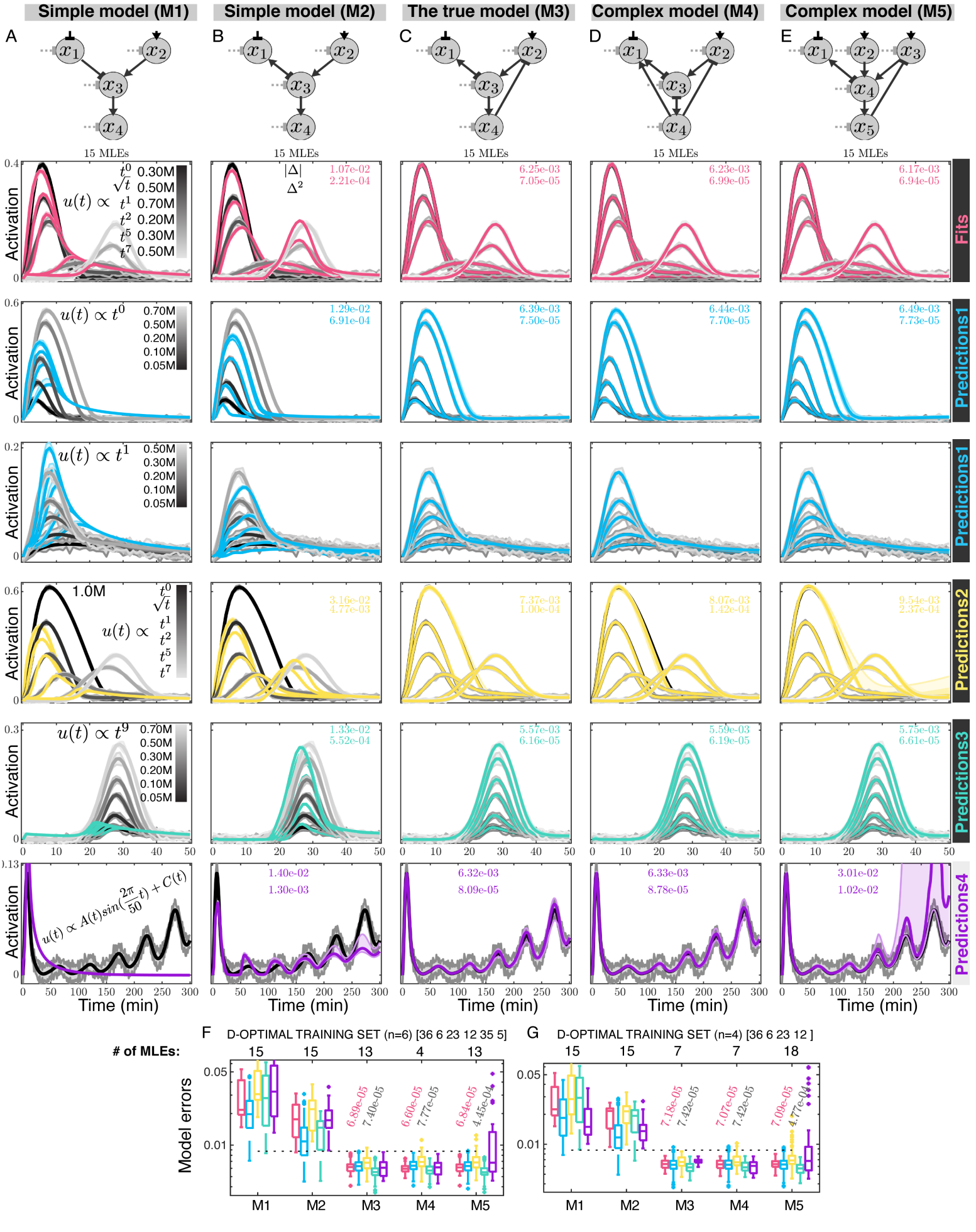
Simple model (M1)
Simple model (M2)
The true model (M3)
Complex model (M4)
Complex model (M5)
A
B
C
D
E
15 MLEs
Activation
Time (min)
Fits
Predictions1
Predictions2
Predictions3
Predictions4
F
G
D-OPTIMAL TRAINING SET (n=6) [36 6 23 12 35 5]
D-OPTIMAL TRAINING SET (n=4) [36 6 23 12]
# of MLEs:
Model errors
M1
M2
M3
M4
M5

Figure S5. Upon diverse kinetics, predictions enable identification of a true model among models of increasing complexities. Related to Figure 5. (A-E) Five models, with increasing complexities from left to right, are compared on the quality of their fits and predictions under data (gray) that are simulated from the true model (M3). From M3 to M2 and to M1, at each step one regulation is removed to generate simpler models. These could represent mutants of M3 where the corresponding kinase activities are removed resulting in loss of feedbacks regulations. From M3 to M4 two extra regulations are added to generate a complex 4-node model. This could represent potential hidden (yet undiscovered) regulations. Finally, M5 is generated by adding a whole new signaling branch (consisting of a sensor node and three regulations) to M3. Second row show MLE fits (reds) of each model compared to the train data (gray). See *STAR Method.* Under parameters constrained for each model from these fits, next rows show model predictions. Mean model errors over each class of data (6 training data in red, 30 testdata1 in blue, 12 testdata2 in yellow, 6 testdata3 in green, 4 testdata4 in purple, as shown in Figure 5J) over all MLEs are given in each panel. The errors correspond to the mean absolute ($|\Delta|$) or the mean squared (Δ^2) difference between the model and data over time. Third row shows models' predictions (examples of P1 in blue) compared to their corresponding testdata1 (steps, gray), and in forth row for linear inputs (blue). Fifth row shows models predictions (examples of P2 in yellow) compared to testdata2 (gray). Sixth row shows models predictions (examples of P3 in green) compared to testdata3 (gray). Seventh row shows models predictions (examples of P4 in purple) compared to testdata4 (gray) upon a sinusoidal oscillatory stimulation that is given in Figure S3H. Shaded plots (red, blue, yellow, green, purple) present 10, 50, and 90 percentiles out of 5 independent fits of each model and their corresponding predictions over time. Quantifications of errors are given in Figure 5. (F-G) Quantification (boxplots) of fit and prediction errors for five models of increasing complexity after training each model with (F) six D-Optimal kinetics and (G) four D-Optimal kinetics that are determined by minimizing the determinant of FIM^{-1} (see *Transparent Methods*). Horizontal dotted black line denotes the standard deviation of the simulated data, and fit/predictions errors (FE/PE) statistics are drawn from training and testing data similar to Figure 5J-5L. For each condition, the mean objective values over training data (red) and over all testing data (gray) are provided in each panel.

Figure S6

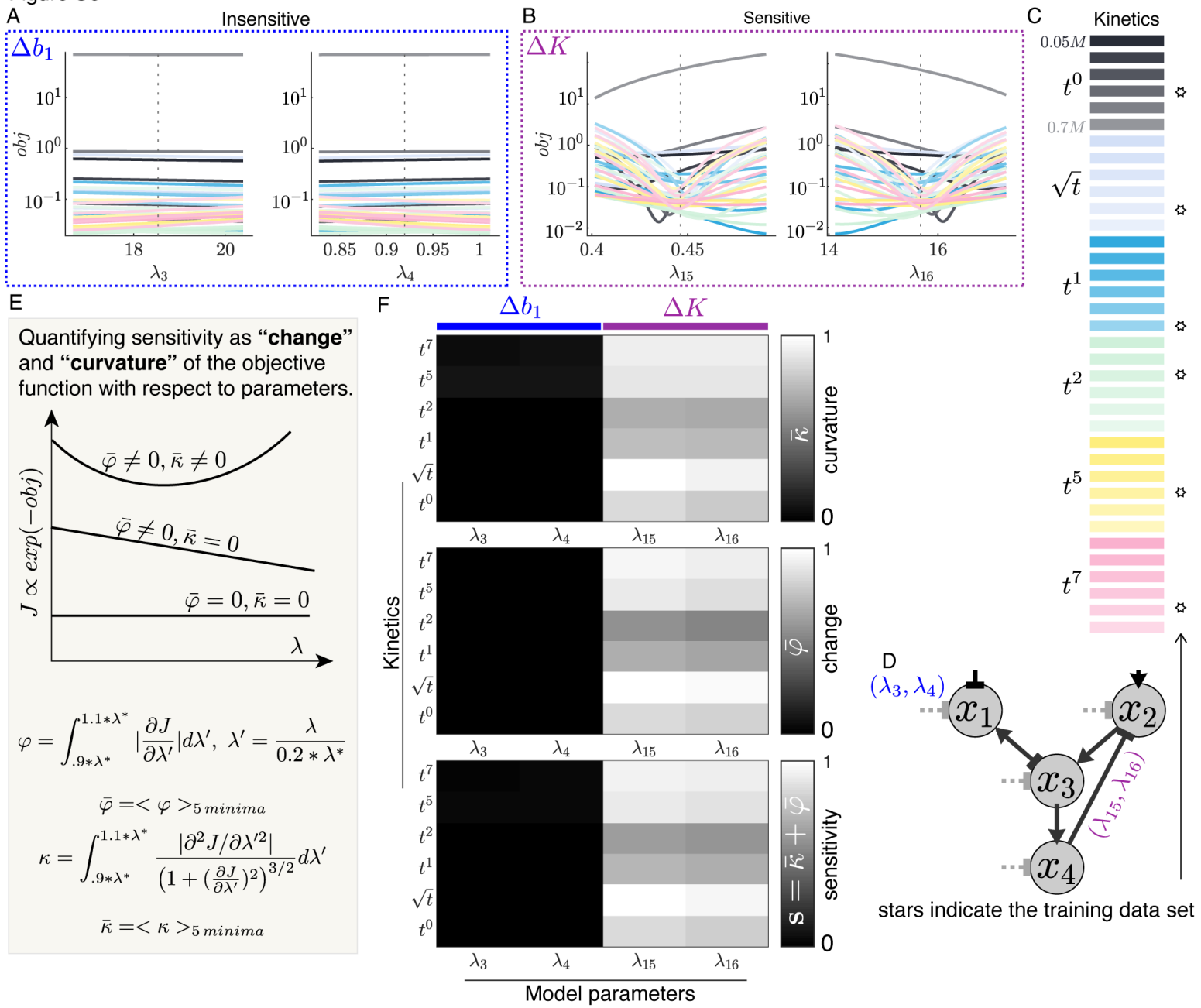
A
Insensitive
Δb_1
B
Sensitive
ΔK
C
Kinetics
$0.05M$
t^0
$0.7M$
$\sqrt{t}$
t^1
t^2
t^5
t^7
obj
λ_3
λ_4
λ_{15}
λ_{16}
D
(λ_3, λ_4)
x_1
x_2
x_3
x_4
$(\lambda_{15}, \lambda_{16})$
stars indicate the training data set
E
Quantifying sensitivity as "change" and "curvature" of the objective function with respect to parameters.
$J \propto exp(-obj)$
$\bar{\varphi} \neq 0, \bar{\kappa} \neq 0$
$\bar{\varphi} \neq 0, \bar{\kappa} = 0$
$\bar{\varphi} = 0, \bar{\kappa} = 0$
λ
$\varphi = \int_{.9*\lambda^*}^{1.1*\lambda^*} |\frac{\partial J}{\partial \lambda'}| d\lambda', \ \lambda' = \frac{\lambda}{0.2 * \lambda^*}$
$\bar{\varphi} =< \varphi >_{5\,minima}$
$\kappa = \int_{.9*\lambda^*}^{1.1*\lambda^*} \frac{|\partial^2 J / \partial \lambda'^2|}{(1 + (\frac{\partial J}{\partial \lambda'})^2)^{3/2}} d\lambda'$
$\bar{\kappa} =< \kappa >_{5\,minima}$
F
Δb_1
ΔK
Kinetics
$\bar{\kappa}$ curvature
$\bar{\varphi}$ change
$\mathbf{s} = \bar{\kappa} + \bar{\varphi}$ sensitivity
Model parameters
G
minimum 1
2
3
4
5
obj versus λ_3
λ_3 (regulation rate of x1 via b1)
H
obj versus λ_{15}
$\times 10^{-3}$
λ_{15} (regulation rate of x2 via x4)

Figure S6. Sensitivity analysis of parameters of the WT model trained upon diverse kinetics allows to screen for mutant responses. Related to Figure 6. (A-D) Sensitivity analysis of WT model with respect to parameters categorizes model parameters into two main groups of insensitive (e.g., λ_3 and λ_4 in A) or sensitive (λ_{15} and λ_{16} in B). In (A and B), the vertical black dotted line indicates the fit value of the corresponding parameter (λ^*), and objective function (Equation S1) is calculated around λ^* upon all kinetic inputs (C). For this analysis, five independent fits are used where WT model (D) is trained with six kinetic input data (indicated with stars in C, similar to training data in Figure 5J). (E) Sensitivity (s), defined as the sum of curvature (κ) and change (derivative, φ) of the objective function with respective to the parameter each integrated around λ^* within 20%. Sensitivity for each model parameter is quantified over 5 independent fits (E) upon all kinetic inputs. It is then marginalized (summed over all final concentrations of each kinetic type) and normalized to the largest sensitivity. (F) For representative parameters, λ_3 and λ_4 (corresponding to **Δ**b$_1$, blue) and λ_{15} and λ_{16} (corresponding to **Δ**K, purple), sensitivity analysis predicts insensitive and sensitive mutants, respectfully. (G-H) An analysis of sensitivity over 5 independent fits indicate that the results are independent of the fits. (G) An example of insensitive parameter (λ_3) preserves this characteristic over all minima while λ_3^* are different across them. (H) Similar result for sensitive parameters (λ_{15}). In (G-H), thick lines are median and shaded area are the interquartile range of all final concentrations for each kinetic type. Colors are according to the bar in (C). This result is consistent for all model parameters across independent fits.

Figure S7

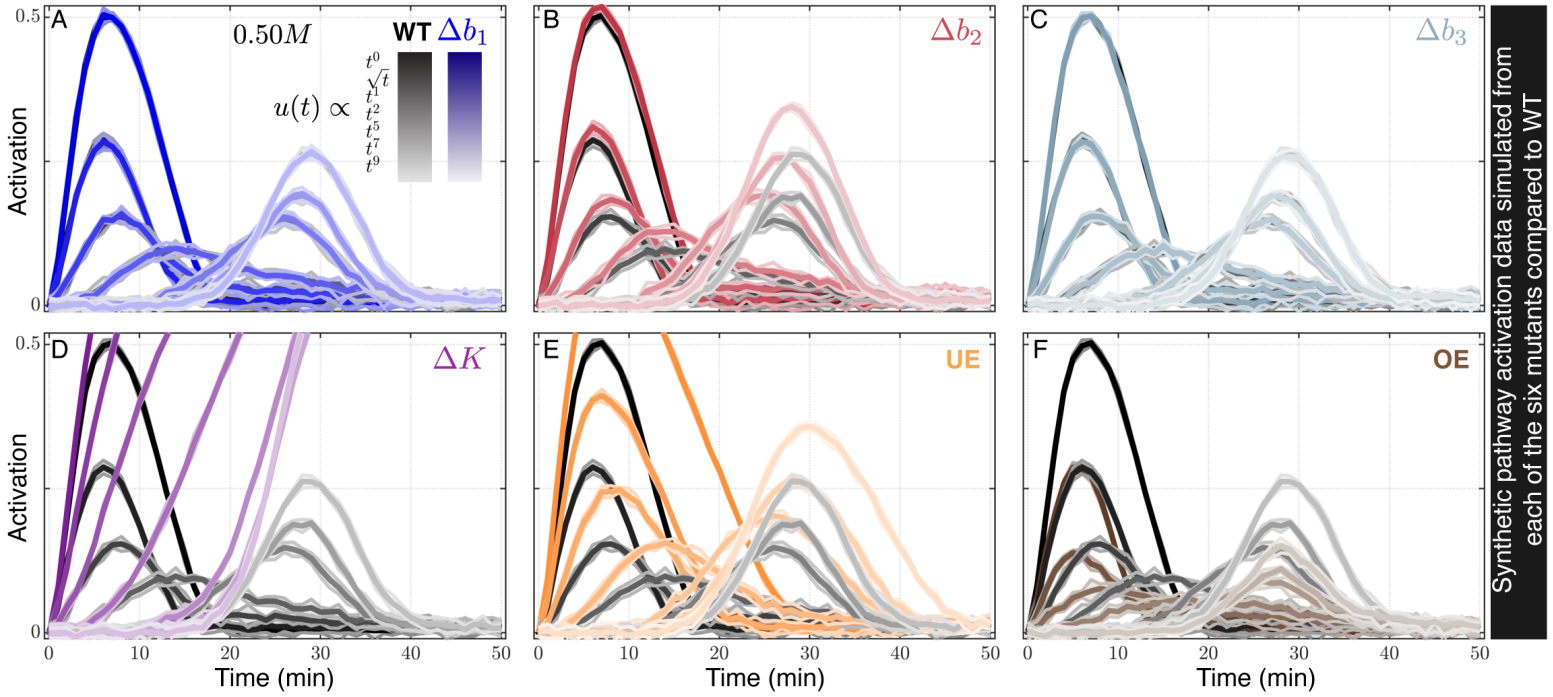

Different final concentrations upon represntative kinetic stimuli of $u(t) \propto t^9$ are shown below for each strain. **Predictions3**

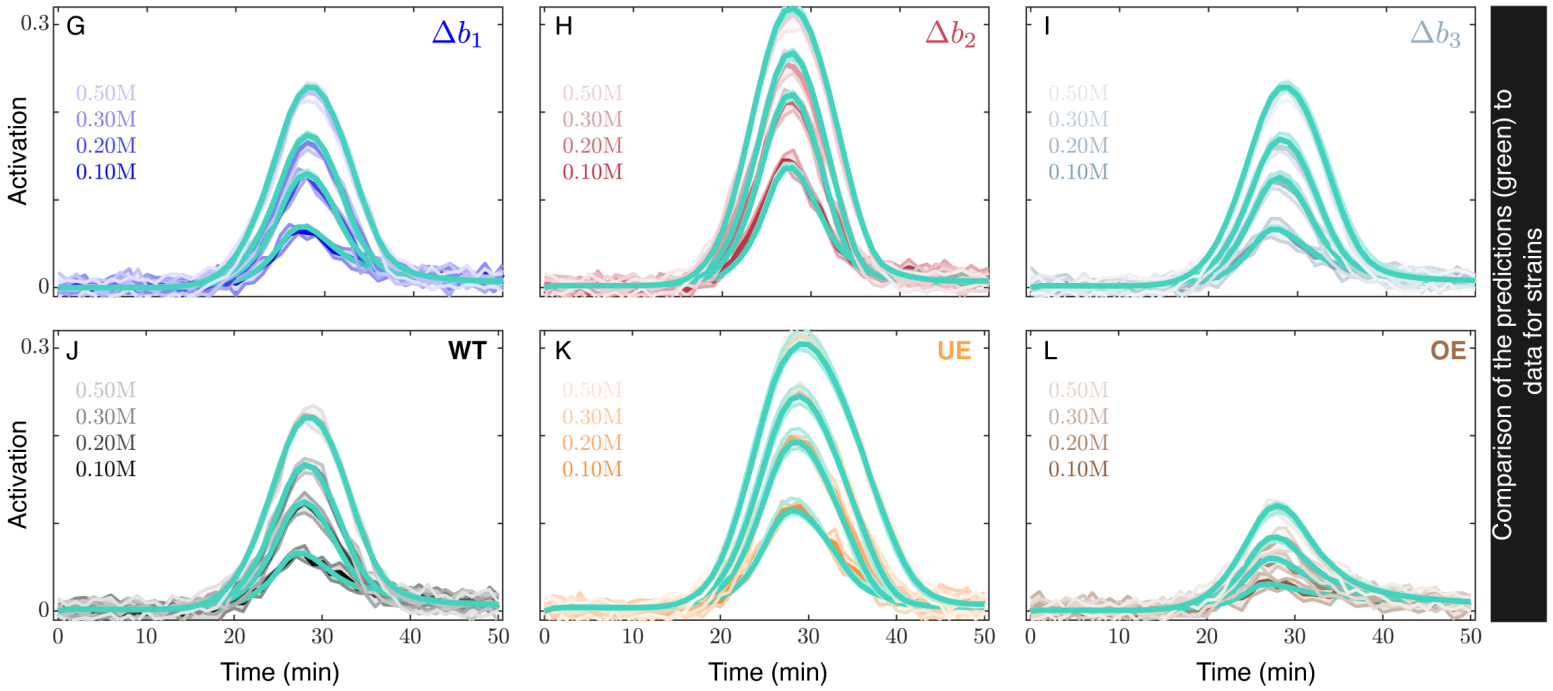

Figure S7. Kinetically diverse stimuli enable to predict mutants' response dynamics. Related to Figure 7. (A-F) Synthetic signaling data simulated from mutated models upon kinetic inputs. Upon diverse kinetics (inset in A) and using parameter set $\boldsymbol{\Lambda}^0$ (Table S1), signaling activations are simulated from six mutants (given in Figure 6A) and each are compared to activation dynamics of WT strain (in gray) (Transparent Methods). Some mutations are insensitive that's indistinguishable from the WT (A,C, **Δ**b_1 and **Δ**b_3) and others are sensitive (B,D-F, **Δ**b_2, **Δ**K, UE, and OE). Sensitivity analysis of WT model with respect to its parameters predicted insensitive (e.g., **Δ**b_1) versus sensitive (e.g., **Δ**K) mutants (Figure 6S). (G-L) Training the WT model on its responses to diverse kinetics enable to accurately predict its mutants' responses. Example pathway activation predictions (predictions3 in green) are compared to their corresponding synthetic data for **Δ**b_1 (G, blue), **Δ**b_2 (H, red), **Δ**b_1 (I, teal), WT (J, gray), UE (K, orange), OE (L, brown) under representative t^9 kinetic inputs. Mutant predictions (green) are generated under $\boldsymbol{\Lambda}^*$ (5 independent best parameter sets constrained by fitting WT model to its kinetically diverse data, Figures 5B and 5J) while mutants synthetic data (blue, red, teal, orange, brown) are simulated under $\boldsymbol{\Lambda}^0$ (Table S1; *Transparent Methods*). Same comparison for the mutant **Δ**K is given in Figure 7D. Quantification of prediction (P1, P2, P3) errors over all 54 kinetics (Figure 1H) for each of the six mutants is given in Figure 7E.

SUPPLMENTAL TABLES

Table S1. Constrained parameter set that was used to simulate all the synthetic data in this paper from WT or mutant models. Related to Figure 1.

$\lambda_1 = 76.866$	$\lambda_6 = 1000.000$	$\lambda_{11} = 0.018$	$\lambda_{16} = 7.639$	$\lambda_{21} = 0.016$
$\lambda_2 = 4.243$	$\lambda_7 = 5.075$	$\lambda_{12} = 0.071$	$\lambda_{17} = 0.019$	$\lambda_{22} = 1.170$
$\lambda_3 = 0.093$	$\lambda_8 = 1000.000$	$\lambda_{13} = 136.332$	$\lambda_{18} = 0.001$	
$\lambda_4 = 941.483$	$\lambda_9 = 0.001$	$\lambda_{14} = 62.558$	$\lambda_{19} = 1.018$	
$\lambda_5 = 0.001$	$\lambda_{10} = 456.755$	$\lambda_{15} = 0.200$	$\lambda_{20} = 4.369$	

These parameters are resulted from fitting the WT model shown in Figure S1K to Hog1 nuclear localization data of two steps of 0.2M and 0.4M simultaneously (Figure S1M). Among 10 fits shown in Figure S1M**,** this parameter set is chosen based on the quality of the predictions of model for pathway activation dynamics.

TRANSPARENT METHODS

Modeling pathway as a dynamic ODE system.

A dynamic Ordinary Differential Equations (ODE) system is used to model the pathway as an enzymatic regulatory network (Figure S1). We developed a general framework that maps any arbitrary regulatory network to their corresponding ODE models implemented in MATLAB 2018a (Figures S1A-S1E). The framework dynamically takes arbitrary number of regulatory nodes in any topology and generates all possible ODE models corresponding to all the possible permutations of the regulations in the network. A convention used in Ref. (Ma et al., 2009) was adopted to formulate the rate equations of the model. Each node in our model represents a protein (or group of proteins) that has a fixed total concentration that can be interconverted between active and inactive states via regulations from either of the kinetic inputs, fixed basal regulators, or other nodes of the network (Figure S1A-S1C). All the regulations that a node receives are summed (Figure S1C), and each regulation (link) is modeled as a Michaelis-Menten function (Figure S1D). In the model, different numbers of nodes could act as sensors to receive extracellular stimulation and these regulators converge on a downstream node which in turn regulate a last node as the readout of the pathway. Each node receives a basal regulation from a source of a fixed concentration. This takes the opposite sign of the overall regulation the node receives from the input or internodes. Such regulation is considered for the role of constitutively active phosphatases and the autoregulation. Finally, feedforward/feedback loop (FFL/FBL) regulations are considered in the most general form in our model, such that complex dynamic behaviors like adaptation are possible. Any realization of such a network with basal regulations and internode regulations (including FFL or FFL regulation) can then be posed as a candidate model for fitting and predicting signaling data (see Figures 5 and S5 as an example).

Despite the apparent topological complexity of signal transduction networks, we focus on a general 4-node topology for the following reasons: i) it is well supported that there might only be a limited number of recurrent network topologies ("circuit motifs") that are capable of robustly executing biological functions (Milo et al., 2002; Shen-Orr et al., 2002; Wagner, 2005). ii) Despite a large number of proteins involved in the signaling networks, multiple of these proteins can be grouped together and considered a virtual node without losing significant generality on the overall pathway activation dynamics and cellular response. Indeed, model reduction methods have been of interest to simplify complex biological systems by exploiting system properties such as signaling activation time scales or parameters sensitivity analysis (Huang et al., 2010; Jeong et al., 2018). iii) Many signaling pathways are *branched* where two (or more) upstream multi-component branches (consisting of the sensors, their phosphorelays, or kinases) are receiving (either the same or different) stimulations through different mechanisms, then converge at a common component, which in turn regulate a terminal signaling protein to trigger proper cellular response. This class of *branched* pathways in their core could be most broadly modeled as a 4-node topology. For example, in the Hog1 MAPK signaling pathway in *S. cerevisiae,* either of the SLN1 or SHO1 branches could be grouped into one virtual node given their fast (millisecond) activation dynamics before they converge on Pbs2 compared to the longer activation dynamics of the Hog1 kinase (that is in the order of 5 minutes) (Saito and Posas, 2012; Tatebayashi et al., 2015).

Simulating synthetic pathway activation dynamics.

To validate the modeling framework and more importantly to establish how model identification depends on the amount and the type of data, synthetic signaling activation dynamics was simulated from a known model in response to different kinetic stimulation profiles. The reason we simulate synthetic data for the part of this paper, in comparison to fully relying on experimentally measured data, is that synthetic data enables to explore how diverse kinetic cell stimulations impacts model identifiability and predictive power, without the obfuscation and potential unknowns that come from modeling experimental data. Challenges in using experimental data could come due to uncertainties in the model, the data, the integration of both, or simply undiscovered biology. Even in the rare cases where both model and measurements may be available, there is still a lack of understanding on how to integrate modeling frameworks with available experimental data such that meaningful new predictions could be made. This is often mainly due to a lack of richness in the collected data that are used to constrain the models. On the other hand, three main reasons make simulating synthetic data ideal for our purpose; i) To study how model predictions depend on data features relies on availability of signaling dynamics over a wide range of kinetics and turning to synthetic data allows to simulate responses upon a wide range of perturbations. ii) Simulating data from a known model provides a ground truth to quantitatively benchmark the performance of a model identification framework while by using experimental data we don't have an underlying known model to cross-check the results. iii) Similar to (ii) simulating synthetic data from a known model with known parameter values provides a reference point to fully parametrize the model. In addition, model performance could be tested in a wide range of parameter space. For these reasons we simulate signaling data under conditions that are biologically inspired and resemble experimental observations.

Among many models that equally fit and predict our Hog1 observation dynamics, a known network topology was chosen that could most broadly represent the class of ubiquitous *branched* signaling pathways and is parametrized through best fit to our available experimental Hog1 activation dynamics upon 0.2M and 0.4M NaCl (Figures S1A, and S1K-S1M). Using the resulting parameters (Table S1), synthetic pathway activation dynamics were generated that qualitatively and quantitatively recapitulate the experimental Hog1 pathway activation dynamics, such as activation levels, measurement noise, onset of activation, maximum activation time and perfect adaptation time (Figures S1 and S2). Upon each stimulation input, single cell trajectories with experimentally realistic noise (to capture cell to cell variability and

measurement noise) were simulated (Figure S1E). We simulated 30 independent synthetic data sets for each condition under independent single-cell noise (Figure S2). We refer to these as 30 “synthetic replicates” of the same data that will be used to initiate 30 independent fits for each condition.

Data for a wider range of stimulations (20 different kinetics to 20 different final concentrations) was performed and conditions shown in Figure 1H were selected under the following criteria: i) to have a stimulation input profile that is physiologically feasible such that it could be generated and delivered to the cells in an experimental setup. Specifically, the solubility of the stimulus in the cell culture media and the operational rates range and precision of the syringe pumps determine the feasibility of generating a desired profile. All the cell stimulation profiles in this manuscript are physiologically feasible and experimentally achievable using the method presented in (Thiemicke et al., 2019). ii) To have a detectable pathway activation response (lower bound on the final concentration), and that the activation shows adaptation and does not saturate (higher bound on the final concentration). iii) To have mutually exclusive (independent) data so that not any pair are overlapping over time for both stimulation inputs and the corresponding pathway responses. This ensures each implemented profile input stimulates the pathway uniquely over time. These criteria guide the generation of biologically inspired synthetic data sets that enable the quantitative investigation of *whether* and *how* the type and the amount of data affect model predictions and model identifiability.

Fitting model to pathway activation data.

We developed a customized optimization algorithm (implemented in MATLAB 2018a) to robustly and rigorously fit a given model to (any number of) pathway activation data to constrain the model parameters. One of the main challenges in parameter optimization is the quality and quantity of available experimental data (Figures 1 and S1). To deal with these limitations, we developed a combinatorial Genetic Algorithm (GA) that efficiently samples a large parameter space, combined with MATLAB’s built in routine *fminsearch* for finer tuning of the parameters at each minimum (Figure S1F). The algorithm dynamically takes a model and a set of training data ($D = \{O_1(t), O_2(t) \dots O_d(t)\}$) and returns a set of parameter sets ($\boldsymbol{\Lambda}^*$) that best fit the training data set (see *next section* in Transparent Methods). For every condition presented, 30 independent fits were performed, each taking one of the 30 “synthetic replicates” of the simulated data along an independent random parameter initiation and resampling through the algorithm (Figure S1G-S1J). This ensures that results are statistically reproducible, that they are not artifacts of noise in the simulated data, and that they are independent of initial parameter guesses. All 30 fit optimizations converged as shown in Figure S1H (objective converges). Fit errors were calculated by comparing each of 30 fits to their corresponding “synthetic replicate” data. These errors were normalized with respect to the number of train data (d) and the number of time points in each data set.

Optimization algorithm.

The algorithm is given in Figure S1F and runs for 21 iterations ($i = \{1,2, \dots 21\}$), which is determined based on fits convergences similar to other algorithm parameters. Each iteration goes through two Genetic Algorithm (GA) calls each followed by a fminsearch (light blue boxes). The first GA and its following fminsearch uses only 25% (selected randomly) of timepoints of each dataset in the train data using ($OBJ25\%$), which helps to escape the potential local minima. Then the second GA and its consequent fminsearch use all timepoints of the train data. We use an objective function as the sum squared errors between the model and data

$$OBJ = \sum_{n=1}^{d} \sum_{t=1}^{N} \frac{\left(x_n(t) - o_n(t)\right)^2}{2\sigma_n(t)^2}, \qquad \text{Equation (S1)}$$

where N is the number of timepoints in each dataset, d is the total number of datasets in the training data, $X_n(t)$ is the model, $O_n(t)$ is the mean, and $\sigma_n(t)$ is the additive noise in the simulated data for dataset n. At the first 4 iterations ($i \leq 4$) as well as at every 4th, the 1st GA takes 200 parameter sets sampled uniformly in [-3,+3] in the logarithmic scale (base

10), and returns a parameter set, which feeds into its following fminsearch. The best parameter sets after the second fminsearch are collected through the iterations, and they are used to resample the 200 parameter sets for the 2nd GA, as well as for the 1st GA for $i > 4$ that's not every 4th (Figure S1F, purple boxes). Each GA runs for 20 generations, passes on 1 elite parameter set at each generation, and uses a custom mutation function that uses the best sets from the last generation (parents) to guess some new parameter sets. Objective values are updated during the 2nd fminsearch if their value is improved. In total, 168,042 (= 2×21×20×200 + 2×21) number of parameter sets are evaluated for each model fit.

Predicting pathway activation dynamics.
From the best parameter sets resulted from fitting the model to a training dataset, the model was solved for $x_4(t)$ (Figure S1E) to simulate the pathway activation prediction under any given stimulation kinetic input. All 30 independent predictions corresponding to 30 independent fits were computed using their corresponding best parameters sets (each of 30 $\boldsymbol{\Lambda}^*$s, Figures S1I and S1J). Prediction errors were quantified by comparing each of 30 predictions to their corresponding "synthetic replicate" data. Prediction errors were normalized with respect to the number of time points.

Simulating synthetic data from mutant pathways.
To evaluate the quality of the predictions upon different extracellular kinetic inputs in the presence of intracellular network perturbations, synthetic data was simulated under all kinetic stimulations from three main classes of mutations in the pathway for the true model, which are i) knockout mutations, ii) varying expression levels, and iii) inhibiting the activity of a protein (Figure 6A). Mutation data was simulated using the same set of parameters ($\boldsymbol{\Lambda}^0$, Table S1) with which the WT pathway activation data was simulated. Three different knockout mutations were generated by eliminating each of the basal regulators (b_1, b_2, and b_3) acting on x_1, x_2, and x_3 nodes. Knockouts are done be setting their corresponding parameters values in the model to zero. Another mutation (e.g., kinase dead) was generated where the activity of the last node (x_4) and thus its regulatory function in terms of feedback on the upstream node x_2 was eliminated by setting their corresponding parameters values in the model to zero. This mutation was expected to show elongated perfect adaptation compared to WT. Finally, overexpression (OE) and underexpression (UE) mutations were generated by changing the concentration of the basal regulator (b_4) acting on x_4. Here b_4 was set to 0.05 (in UE) and 0.20 (in OE) compared to b_4 =0.10 of WT (a two-fold change for each). From each of the 6 mutated pathways of the true model, their corresponding activation dynamics, $O(t) \propto x_4(t)$, was simulated under all the kinetic stimulation inputs (shown in Figure 1H), and representative activation dynamics for each mutant are shown in Figures S7A-S7F.

Predicting pathway activation dynamics for mutated pathways.
For each of the 6 mutants, the best parameter sets ($\boldsymbol{\Lambda}^*$) after training the WT model were used to generate the mutants' corresponding predictions under each extracellular kinetic input (Figures 6A and S7). For this task, the 5 lowest objective $\boldsymbol{\Lambda}^*$ resulting from the 30 independent fits using GA-fminsearch given in Figure S1F-S1J are used. For all results presented in this study on mutants, all $\boldsymbol{\Lambda}^*$s are obtained by only training the WT pathway with its six dynamically different signaling responses; no mutant models or data were used for fitting. The WT model is given in Figure 5B and the training data is given in Figure 5J.

Fisher Information Matrix (FIM) analysis to estimate parameter uncertainties.
The Fisher information matrix (FIM) analysis was used to estimate expected parameter uncertainty for different experiment designs (Apgar et al., 2010; Fox and Munsky, 2019; Hagen et al., 2013; Jetka et al., 2018; Komorowski et al., 2011). The FIM provides the amount of information an observable could provide around an unknown parameter, and it has been extensively used to estimate how well potential experiments will constrain model parameters (Apgar et al., 2008; Bandara et al., 2009; Fox and Munsky, 2019; Sinkoe and Hahn, 2017; Stewart-Ornstein et al., 2017). The FIM^{-1}, the

inverse of the FIM, known as the Cramer-Rao bound (CRB), is in particular useful as it provides a lower bound on the variance for any unbiased estimator of model parameters (Aitkin, 2010).

For any given model (Equation S2, Figure S1C), sensitivity equations for all model parameters (Equation S3) are

$$
\begin{array}{ll}
d\mathbf{x}/dt = \mathbf{f}(\mathbf{x}, \mathbf{b}, \mathbf{\Lambda}, u(t), t); & \text{model ODE} \\
\mathbf{x} = \{x_1(t), x_2(t), \ldots x_N(t)\}, & \text{N regulatory proteins} \\
\mathbf{b} = \{b_1, b_2, \ldots b_N\}, & \text{N basal regulators} \\
\mathbf{f} = \{f_1, f_2, \ldots f_N\}, & \text{N regulatory rate functions} \\
\mathbf{\Lambda} = \{\lambda_1, \lambda_2, \ldots \lambda_M\}, & \text{M model parameters}
\end{array}
\qquad \text{(Equation S2)}
$$

$$
\begin{array}{ll}
\mathbf{S} = \Delta_{\mathbf{\Lambda}}\mathbf{x} = \int \Delta_{\mathbf{\Lambda}}\mathbf{f}(\mathbf{x}, \mathbf{b}, u(t), t; \mathbf{\Lambda})dt, & \text{Sensitivity} \\
\frac{d\mathbf{S}}{dt} = \Delta_{\mathbf{\Lambda}}\mathbf{f}(\mathbf{x}, \mathbf{b}, u(t), t; \mathbf{\Lambda}) + \mathbf{J}(\mathbf{x}, \mathbf{b}, u(t), t; \mathbf{\Lambda})\mathbf{S}, & \text{Sensitivity ODE}
\end{array}
\qquad \text{(Equation S3)}
$$

$$
\frac{d}{dt}\begin{pmatrix}\mathbf{x} \\ \mathbf{S}_i\end{pmatrix} = \begin{pmatrix}\mathbf{f}(\mathbf{x}, \mathbf{b}, \mathbf{\Lambda}, u(t), t) \\ \Delta_{\lambda_i}\mathbf{f}(\mathbf{x}, \mathbf{b}, u(t), t; \mathbf{\Lambda}) + \mathbf{J}(\mathbf{x}, \mathbf{b}, u(t), t; \mathbf{\Lambda})\mathbf{S}_i\end{pmatrix} \quad \text{Joint model and sensitivity ODE} \qquad \text{(Equation S4)}
$$

$$
\mathbf{S} = \begin{pmatrix} \frac{\partial x_1}{\partial \lambda_1} & \frac{\partial x_1}{\partial \lambda_2} & \cdots & \frac{\partial x_1}{\partial \lambda_M} \\ \frac{\partial x_2}{\partial \lambda_1} & \frac{\partial x_2}{\partial \lambda_2} & \cdots & \frac{\partial x_2}{\partial \lambda_M} \\ . & . & & . \\ \frac{\partial x_N}{\partial \lambda_1} & \frac{\partial x_N}{\partial \lambda_2} & \cdots & \frac{\partial x_N}{\partial \lambda_M} \end{pmatrix}, \qquad \text{Sensitivity matrix}
$$

$$
\mathbf{J} = \begin{pmatrix} \frac{\partial f_1}{\partial x_1} & \frac{\partial f_1}{\partial x_2} & \cdots & \frac{\partial f_1}{\partial x_N} \\ \frac{\partial f_2}{\partial x_1} & \frac{\partial f_2}{\partial x_2} & \cdots & \frac{\partial f_2}{\partial x_N} \\ . & . & & . \\ \frac{\partial f_N}{\partial x_1} & \frac{\partial f_N}{\partial x_2} & \cdots & \frac{\partial f_N}{\partial x_N} \end{pmatrix}, \qquad \text{Jacobian matrix}
$$

$$
\Delta_{\mathbf{\Lambda}}\mathbf{f}(\mathbf{x}, \mathbf{b}, u(t), t; \mathbf{\Lambda}) = \begin{pmatrix} \frac{\partial f_1}{\partial \lambda_1} & \frac{\partial f_1}{\partial \lambda_2} & \cdots & \frac{\partial f_1}{\partial \lambda_M} \\ \frac{\partial f_2}{\partial \lambda_1} & \frac{\partial f_2}{\partial \lambda_2} & \cdots & \frac{\partial f_2}{\partial \lambda_M} \\ . & . & & . \\ \frac{\partial f_N}{\partial \lambda_1} & \frac{\partial f_N}{\partial \lambda_2} & \cdots & \frac{\partial f_N}{\partial \lambda_M} \end{pmatrix}, \quad \begin{array}{l}\text{Partials of rate functions} \\ \text{with respect to model parameters}\end{array}
$$

$$
\mathbf{FIM}(log\mathbf{\Lambda})_{ij} = (\lambda_i\lambda_j)\mathbf{S}_i^T\mathbf{\Sigma}^{-1}\mathbf{S}_j \qquad \text{Fisher Information Matrix (FIM)} \qquad \text{(Equation S5)}
$$

formulated and are solved along the model ODEs (Equation S4) using Jacobian matrix of the rate functions under the initial and boundary conditions given in Figure S1E. Logarithmic parametrization of FIM is then computed to estimate the relative sensitivity of the parameters.

From each model fit (to any set of train data), around each resulting best parameter set ($\mathbf{\Lambda}^*$, Figure S1I) the FIM and its inverse, FIM^{-1}, are computed upon all stimulation inputs. For each test data, standard deviation of the simulated activation dynamics over time, resulted from additive Gaussian noise that is independent of the mean activation (Figure S1E), is used to build the diagonal covariance matrix (Σ), which is used along computed sensitivities to calculate FIM (Equation S5). Several different metrics of the FIM, known as Optimality analysis, that are standard in model-guided experiment design are used to evaluate uncertainties (Fox and Munsky, 2019). These include A-Optimality, E-Optimality, T-Optimality, and D-Optimality, where the choice of the specific criteria depends on the application under the study. For example, E-Optimality corresponds to the smallest eigenvalue of the FIM, therefore gives a measure on how well an experiment design constrains the principle direction of parameter space that has the highest uncertainty. D-optimality, which corresponds to the determinant of the FIM provides a measure of the volume of the uncertainty in parameter space, therefore is best suited for our purpose to compare different experiments in their ability to constrain the model parameters.

We defined a custom optimality "W-Optimality" as a weighted sum over the uncertainties (Δ^i) estimated by FIM^{-1} for individual parameters of the model (Figures S4L-S4O). In particular, this optimality gives more weight to better constrained parameters and less weight to insensitive ones, therefore it could provide a more accurate estimate of a specific experiment design in constraining the parameters that matters most by excluding the contribution of the sloppy parameters.

Under models fit to five different experiment designs that have the same amount of data (six steps, six linears, six quadratics, six diverse kinetics of 0.30M or six diverse kinetics of 0.70M), the FIM is calculated upon all test data. Then, the resulted FIM or FIM^{-1} was used to estimate the uncertainty of the model parameters using optimality metrics described above. Uncertainty estimated by each optimality is summed over all of testdata1, testdata2, or testdata3 kinetic stimulations and the results for 10 independent fits are shown in Figures 4F, 4G and S4L-S4O. The estimates of the model uncertainty for five different experiment designs computed using a representative kinetic input (t^9, 0.7M) from 10 independent fits are shown in Figures 4F-4G for D-Optimality. A comprehensive analysis of the model uncertainty for all optimality criteria described above and using all kinetic stimulations are given in Figures S4L-S4N.

Maximum Likelihood Estimates (MLEs).

We employed a Maximum Likelihood Estimate (MLE) to verify our FIM approach. For computational tractability of solving the model ODEs and the fact that the MLEs are difficult to converge at higher dimensions, we limited the FIM verification to four free parameters (the remaining parameters were fixed to their true values). 1000 trajectories were simulated for each experimental design (each training datasets) and Gaussian noise was added. For these 1000 simulated trajectories, 1000 MLE fits (one MLE per trajectory) were initiated from a multivariate distribution centered at the true parameters and distributed with a covariance matrix equal to the inverse FIM. For MLEs, we employed the MATLAB built-in fminsearch with the objective function as the log-likelihood function (i.e., the sum of squared deviations) between the model and data (Equation S1). For each data set, the corresponding MLEs search was verified for convergence by checking that its final objective value was lower than that using either the true parameter set or any other parameter set found by fitting a different simulated data set. MLE fits that did not converge were discarded. The MLE results are compared against FIM in Figures 4C-4E and S4J, S4K.

Bayesian analysis.

We employed a Bayesian analysis to quantify the posterior uncertainty of parameters for the homogenous inputs compared to those of the diverse input signals. The algorithm is as follows; under each training dataset, 10 parallel chains were initiated each sampling 5000 parameters sets with a uniform prior [-3, +3] in logarithmic space (base 10) under a randomized rng seed in MATALB. Using MATLAB parpool, the model ODEs (Figures S1A-S1E) were solved for the signaling activation upon training data inputs for all sampled parameters sets, and their corresponding objective values were quantified as the mean squared errors between the model and data (Equation S1). All parameter sets were weighted by their likelihoods and their weighted means and covariance were quantified. The likelihood function L(Λ) is defined as:

$$L(\Lambda) = \frac{\exp\left(-OBJ(\Lambda)/\alpha\right)}{\sum \exp\left(-OBJ(\Lambda)/\alpha\right)}, \qquad \text{(Equation S6)}$$

where OBJ is given in Equation S1. The OBJ is divided by a constant factor ($\alpha = 300$) to scale the likelihood function to avoid the dominance of few parameter sets. From a multivariate distribution centered at the weighted mean parameters with weighted covariance matrix, 5000 parameters sets were resampled. Each chain was then evolved through 1000 iterations of this procedure until the total objective and parameters statistics had converged. As an inertia in updating fit search, at each iteration (i), the mean (μ_i) and the covariance matrix (Σ_i) were weighted with their values from the previous iteration according to

$$\mu_i = 0.5 * \mu_i + 0.5 * \mu_{i-1} \qquad \text{(Equation S7)}$$

$\Sigma_i = 0.5 * \Sigma_i + 0.5 * \Sigma_{i-1}$,

and during the first 500 iterations, a small term (equal to 0.001 for Figure 4E and 0.01 for Figures 4J-4L) was added to the diagonal of the covariance to help to explore the parameter space. From converged chains, prediction errors on novel input signals were then quantified using 100 parameters sets sampled according to the posterior distribution for each chain. The chains are kept under convergence criteria of <FE> <= d_std, where <FE> is the average fit error under all sampled parameters from the posterior upon all training data sets and d_std is the standard deviation of the data. The results are provided in Figures 4J-4L.

Model Identification.

Model identification was performed around a set of parameters set (Λ^{start}) that was determined as following; Λ^{start} was obtained for simple models (M1 and M2) by parametrizing these models using the GA-fminsearch optimization algorithm in Figure S1F ($\Lambda^{start} = \Lambda^*$ of lowest objective value out of 30 independent fits), while for the true and the more complex models (M3-M5), Λ^{start} was set to the true parameters (Λ^0) with small values (-3 in log10 scale) for the nested parameters in M4 and M5. For each condition, 60 MLEs were performed starting from parameter sets that were sampled from a multivariate distribution centered at Λ^{start} and distributed with a covariance matrix equal to the inverse FIM for that model. For computational tractability, this analysis was performed under odd free model parameters for both FIM calculations and MLEs (the remaining parameters were fixed to their true values). For MLEs of M1-M3, the goal objective was set as that of the true parameters in M3, and for MLEs of M4-M5, the goal objective was set as that of M3 MLEs. For M1-M2, the best 15 MLEs are kept, for M3 the converged parameter sets by checking that their final objective values were lower than that using the true parameter set. For M4-M5 the parameter sets with objective values at least as low as that of M3 MLEs that are converged were kept. From each model using the resulting parameter sets, predictions on novel input signals were then made. The results are provided in Figures 5 and S5.

Mutation severity.

For each mutant, mutation severity is computed as the sum of absolute difference in activation dynamics of a mutant from that of the WT over time upon all kinetic stimulations (Figure 6D). The mutation severity was marginalized for each kinetic type (summed over all final concentrations for each type kinetics), then normalized to the largest severity.

Experiments, image processing, and data analysis to measure Hog1 dynamics.

Yeast *Saccharomyces cerevisiae* BY4741 was used for time-lapse microscopy. To assay the nuclear enrichment of Hog1 in single cells over time in response to NaCl osmotic stress, a yellow-fluorescent protein (YFP) was tagged to the C-terminus of endogenous Hog1 in BY4741 cells through homologous DNA recombination. A computer programmed syringe pump is used to control the osmatic stress over cells using a flowchamber (Thiemicke et al., 2019). The number of biological replicates (BR) and single cells presented in Figures 1B and 1C are as following; control has 6 BRs that have 6, 22, 5, 21, 9, and 9 cells; step 0.2M has 3 BRs that have 22, 53, and 67 cells; step 0.4M has 3 BRs that have 23, 25, and 42 cells; linear 0.4M 10min has 3 BRs that have 25, 9 and 45 single cells; quadratic 0.4M 10min has 3 BRs that have 67, 53 and 61 single cells.

SUPPLEMENTAL REFERENCES

Aitkin, M. (2010). Statistical Inference: An Integrated Bayesian/Likelihood Approach (Chapman & Hall/CRC).

Apgar, J.F., Toettcher, J.E., Endy, D., White, F.M., and Tidor, B. (2008). Stimulus design for model selection and validation in cell signaling. PLoS Comput. Biol. *4*, e30.

Apgar, J.F., Witmer, D.K., White, F.M., and Tidor, B. (2010). Sloppy models, parameter uncertainty, and the role of experimental design. Mol. Biosyst. *6*, 1890.

Bandara, S., Schlöder, J.P., Eils, R., Bock, H.G., and Meyer, T. (2009). Optimal experimental design for parameter

estimation of a cell signaling model. PLoS Comput. Biol. *5*, e1000558.
Fox, Z.R., and Munsky, B. (2019). The finite state projection based Fisher information matrix approach to estimate information and optimize single-cell experiments. PLOS Comput. Biol. *15*, e1006365.
Hagen, D.R., White, J.K., and Tidor, B. (2013). Convergence in parameters and predictions using computational experimental design. Interface Focus *3*, 20130008.
Huang, Z.J., Chu, Y., and Hahn, J. (2010). Model simplification procedure for signal transduction pathway models: An application to IL-6 signaling. Chem. Eng. Sci. *65*, 1964–1975.
Jeong, J.E., Zhuang, Q., Transtrum, M.K., Zhou, E., and Qiu, P. (2018). Experimental design and model reduction in systems biology. Quant. Biol. *6*, 287–306.
Jetka, T., Nienałtowski, K., Filippi, S., Stumpf, M.P.H., and Komorowski, M. (2018). An information-theoretic framework for deciphering pleiotropic and noisy biochemical signaling. Nat. Commun. *9*, 4591.
Komorowski, M., Costa, M.J., Rand, D.A., and Stumpf, M.P.H. (2011). Sensitivity, robustness, and identifiability in stochastic chemical kinetics models. Proc. Natl. Acad. Sci. U. S. A. *108*, 8645–8650.
Ma, W., Trusina, A., El-Samad, H., Lim, W.A., and Tang, C. (2009). Defining network topologies that can achieve biochemical adaptation. Cell *138*, 760–773.
Milo, R., Shen-Orr, S., Itzkovitz, S., Kashtan, N., Chklovskii, D., and Alon, U. (2002). Network motifs: simple building blocks of complex networks. Science *298*, 824–827.
Saito, H., and Posas, F. (2012). Response to hyperosmotic stress. Genetics *192*, 289–318.
Shen-Orr, S.S., Milo, R., Mangan, S., and Alon, U. (2002). Network motifs in the transcriptional regulation network of Escherichia coli. Nat. Genet. *31*, 64–68.
Sinkoe, A., and Hahn, J. (2017). Optimal experimental design for parameter estimation of an IL-6 signaling model. Processes *5*, 49.
Stewart-Ornstein, J., Chen, S., Bhatnagar, R., Weissman, J.S., and El-Samad, H. (2017). Model-guided optogenetic study of PKA signaling in budding yeast. Mol. Biol. Cell *28*, 221–227.
Tatebayashi, K., Yamamoto, K., Nagoya, M., Takayama, T., Nishimura, A., Sakurai, M., Momma, T., and Saito, H. (2015). Osmosensing and scaffolding functions of the oligomeric four-transmembrane domain osmosensor Sho1. Nat. Commun. *6*, 6975.
Thiemicke, A., Jashnsaz, H., Li, G., and Neuert, G. (2019). Generating kinetic environments to study dynamic cellular processes in single cells. Sci. Rep. *9*, 10129.
Wagner, A. (2005). Circuit topology and the evolution of robustness in two-gene circadian oscillators. Proc. Natl. Acad. Sci. U. S. A. *102*, 11775–11780.